UNIVERSITY OF CALIFORNIA, SAN DIEGO

Superconducting vortex pinning with artificially prepared nanostructures

A dissertation submitted in partial satisfaction of the requirements for the degree

Doctor of Philosophy

in

Physics

by

Yaniv Jacob Rosen

Committee in charge:

Professor Ivan K. Schuller, Chair
Professor Daniel P. Arovas
Professor Eric Fullerton
Professor Shayan Mookherjea
Professor Oleg G. Shpyrko

2013

The Dissertation of Yaniv Jacob Rosen is approved, and it is acceptable in quality and form for publication on microfilm and electronically:

Chair

University of California, San Diego

2013

DEDICATION

Dedicated to my parents

TABLE OF CONTENTS

LIST OF ABBREVIATIONS

- LHe – Liquid Helium
- E-beam – Electron Beam
- PCF – Pair correlation function
- RLO – Range of local order
- SEM – Scanning electron microscope
- MFM – Magnetic force microscope
- PDE – partial differential equation

LIST OF FIGURES

LIST OF TABLES

ACKNOWELDGEMENTS

This dissertation would not have been possible without the help of many friends and colleagues.

Primarily I would like to thank my advisor, Prof. Ivan K. Schuller, for all his help and encouragement throughout my graduate career. Whenever I was stuck, he always had ideas and a new way of thinking about the problem. He not only taught me how to do research, but also how to present it to my audience by making the research relevant to different people. Most importantly though, Ivan taught me how to critique ideas and ask questions. He constantly exposed me to examples of bad science and questionable techniques with the purpose of learning from them and avoiding suspicious research projects. Ivan constantly challenged me to become a better researcher and taught me how to do good research.

I would also like to thank the postdocs who helped teach me to do research. In particular, Amos Sharoni, who mentored me and taught me the fundamentals of working in a lab. He taught me how to write papers and how to come up with interesting project ideas. I would also like to thank Stefan Guénon for constantly pushing me to examine my assumptions and better describe my methods. Discussions with him have helped me become much more careful in my fabrication methods, clearer in my descriptions, and thorough in my background research.

Stefan Guénon also greatly helped me with the corrections for this dissertation. Thomas Saerbeck and Jason Leonard were also instrumental in the

writing of this dissertation, haranguing me constantly to be more precise with my language and to remove colloquialisms.

Professor Jose Vicent was always helpful and supportive. He generously agreed to write me a letter of recommendation. I would like to thank him and his colleagues, David Perez de Lara, and Elvira González.

I would like to thank our one-time group members Igor Roshchin, Thomas Gredig, Javier Villegas, and Felix Casanova who were always happy to help me with problems around the lab. I would also like to thank my colleagues Juan Viterbo, Ilya Valmianski, Siming Wang, Carlos Monton, Ali Basaran, Corneliu Colesniuc, Jose De La Venta, Gabriel Ramirez, Christian Urban, Misha Erekhinsky, Kevin West, and Samuel Hevia. They were always willing to give me advice, listen to a practice talk, scrutinize a mathematical argument, or go to coffee when I needed a break.

I thank Michael Anderson and Oleg Shpyrko for their help and support with the young physicist program. I thank Jonathan Bent and Alex Winbow for keeping me sane, and Eric Michelson and Shimshon Barad for very entertaining physics discussions. I am also grateful for the help from Hilari Ford, Sharmila Poddar, Kevin Smith, Robin Knox, Lester Brooks, Simone Radice, and Jeff Phillips, I could not have finished without their support.

I am very thankful for the love and support of my Grandparents, my cousin Michael, and my girlfriend Kendall Dodds. I would especially like to thank my parents. Their love and encouragement have allowed me to reach this point today.

Chapter II, in part has been previously published in: Y. J. Rosen, A. Sharoni, and Ivan K. Schuller, “Enhanced superconducting vortex pinning with disordered nanomagnetic arrays,” Phys. Rev. B 82, 014509 (2010). The dissertation author was the primary investigator and author of this material. Y. J. Rosen selected the experiment and algorithm to use, fabricated the samples, performed the analysis and was the primary author on the paper.

Chapter III has been published in: D. Perez de Lara, M. Erekhinsky, E. M. Gonzalez, Y. J. Rosen, Ivan K. Schuller, and J. L. Vicent, “Vortex ratchet reversal: Role of interstitial vortices,” Phys. Rev. B 83, 174507 (2011). The dissertation author was a co-author of this paper. I would also like to thank Alicia Gomez for help with the errata for the paper. Y. J. Rosen fabricated samples for this project, corrected the length scales in the paper, wrote the errata, and worked on the explanations for the data.

Chapter IV is currently being prepared for publication. Co-authors include S. Guenon and Ivan K. Schuller. The dissertation author was the primary investigator and author of this material. Y. J. Rosen worked on the sample design, performed the fabrication, measurement, analysis, and simulation for this work, and will be the primary author on the paper.

Chapter V contains work performed with several collaborators. I would like to thank Carlos Monton, Ilya Valmianski, and Juan Pererio for the fabrication of the porous alumina. I would like to thank Amos Sharoni for useful conversations and

advice in regards to section ‘V.1 Pinning boundary effects’. I would also like to thank Stefan Guenon for the conformal mapping experiments. I would like to thank Santiago Carreira, Claudio Chiliotte, and Victoria Bekeris for measurements in regard to section ‘V.2 Magnetic susceptibility measurements’. I would like to thank Qiang Wang and Mike Fitzimmonds for measurements in regards to section ‘V.3 Neutron scattering’. I would like to thank Sergio Montoya, Matthias Gottwald, and Eric Fullerton for measurements in regard to section ‘V.4 Magnetic force microscopy of the vortex lattice’. Finally, I would like to thank Cynthia and Charles Reichhardt for useful conversations and advice in regards to section ‘V.5 Simulating the vortex lattice’. Y. J. Rosen performed the fabrication and measurements in V.1. Y. J. Rosen assisted in the fabrication of the samples, and is providing the theoretical background for section V.2, V.3, and V.4. Y. J. Rosen performed the simulations in V.5.

The work presented in this dissertation was funded by the National Science Foundation Grant #DMR-0800207. I want to thank them for their generous support.

VITA

2004 Associate of Science, Physics and Mathematics, Foothill College, Los Altos, CA

2006 Bachelor of Arts, Physics and Mathematics, University of California, Berkeley, Berkeley, CA

2008 Master of Science, Physics, University of California, San Diego, La Jolla, CA

2013 Doctor of Philosophy, Physics, University of California, San Diego, La Jolla, CA

ABSTRACT OF THE DISSERTATION

Superconducting vortex pinning with artificially prepared nanostructures

by

Yaniv Jacob Rosen

Doctor of Philosophy in Physics

University of California, San Diego, 2013

Professor Ivan K. Schuller, Chair

Vortex pinning in superconductors with artificially introduced pinning arrays provides a controllable method for studying periodic systems moving in the presence of a periodic potential. Vortex pinning has applications that include enhancing critical current densities for superconducting transmission lines and reducing noise in a variety of devices based on superconductivity. Modern nanolithography enables the positioning of pinning structures at length scales similar to the vortex interaction

length in superconductors. This provides the means to manipulate the potential-energy landscape and to study vortex dynamics under tunable conditions.

Although the role of disorder and defects in a lattice is of great importance in condensed-matter physics, it has received little attention in the context of vortices. While the extreme case of intrinsic defects lacking any order has previously been studied, there have been few attempts to study partially ordered systems. This dissertation studies the effects on the vortices of different types of controlled partial order in pinning site lattices.

Experiments clarifying the origin of the ratchet effect in vortex systems have been performed. It has previously been shown that in a non-symmetric vortex potential, an AC current can be applied to a superconducting system and a DC voltage will emerge. The DC voltage can undergo a ratchet reversal, where the sign of the DC voltage changes. An experiment testing the origin of the DC ratchet reversal has been performed and compared to several theories.

The effects of different current density configurations are explored in circular geometries. In the Corbino geometry, current is injected in the center of a superconducting disc and travels radially outwards towards the edges causing a tangential shearing force on the vortex lattice. This dissertation studies the Corbino geometry in the presence of different periodic potentials, and shows that the vortex lattice undergoes a shearing transition due to the pinning sites.

Finally, several ongoing projects and international collaborations are presented. Measurements of the vortex lattice using microwave magnetic susceptibility measurements, neutron scattering, and magnetic force microscopy are discussed. A computer simulation of the vortex lattice is presented, and an experiment involving varying pinning site densities is described.

CHAPTER I

INTRODUCTION

I.1 Superconducting vortex pinning

The field of superconductivity has a rich spectrum of applications and open research questions [1]. The interaction of type II superconductors with magnetic fields is particularly striking. Quantized units of flux surrounded by vortices of current can form inside the superconductor [2] creating a macroscopic example of quantum mechanics. Not only is this affect a possible implementation of quantum computing [3], but it also has many other applications. For example, pinning of superconducting vortices provides a controllable method for studying a periodic system moving in the presence of a periodic potential. These conditions appear in various places including the interaction between epitaxial films [4], confined charged plasmas [5], and biological ratchets [6]. Artificial pinning sites have allowed a number of new phenomena to be engineered into superconducting systems such as field-driven superconductivity [7], bistability [8], ratchet effects [9], and new Josephson effects [10]. This type of pinning structure may also provide the means for understanding pulsar glitches in neutron stars [11], enhancing critical current densities for superconducting transmission lines [12,13], reducing noise in a variety of superconductivity based devices [14], and enhancing magnetic levitation [15].

This dissertation studies vortex dynamics in artificial pinning potentials using various techniques and geometries. The exploration of these dynamics can illuminate the collaborative effects between vortices and allow better control of their mobility in superconductors. Furthermore, several novel phenomena are studied that could lead to devices in superconducting systems.

The dissertation is organized as follows. Chapter I gives a brief theoretical background on vortex physics and the measurement techniques used. Chapter II describes interactions between vortex lattices and disordered pinning lattices. Chapter III discusses experiments to determine the origin of the ratchet effect. Chapter IV contains an experiment using a particular type of measurement structure called the Corbino geometry [16]. Chapter V contains a brief summary of ongoing and past projects including those with international collaborators. Finally, chapter VI contains a brief summary of the finding presented in this dissertation and chapter VII contains the bibliography.

I.2 Vortex theory

I.2.1 Type I and II superconductors

One defining characteristic of superconductivity is the Meissner effect [1,2,17]. When a type I superconductor is cooled through its transition, magnetic field is expelled from the superconductor and it becomes perfectly

diamagnetic. This situation is distinct from a perfect conductor where the zero resistance state only prevents a change of the magnetic field.

When a magnetic field is applied to a type I superconductor it is expelled by surface currents. This happens for all magnetic fields up to some critical field, H_C, after which it becomes a normal metal (Figure 1a). Because the expulsion of magnetic field is a surface effect, there is a parameter, λ, which governs the magnetic field penetration depth into the surface of the superconductor.

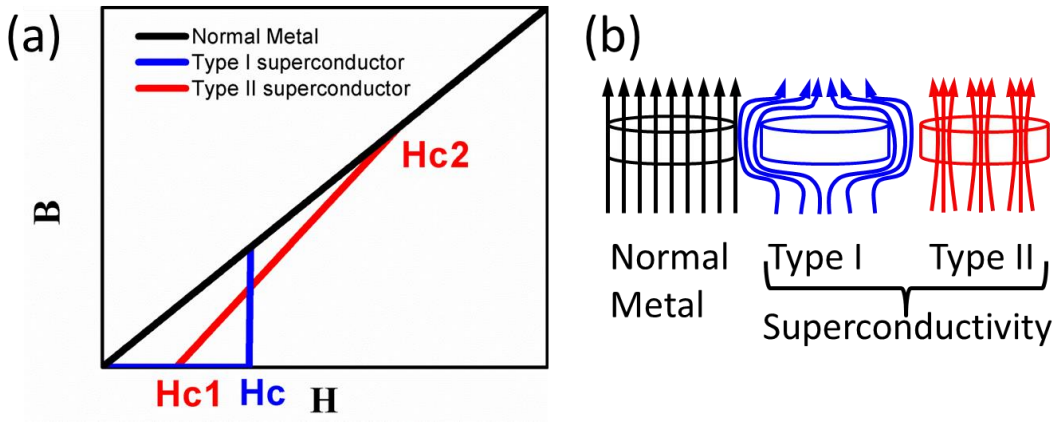

Figure 1. (a) B-field as a function of the external applied magnetic field, H, inside a normal metal, a type I, and a type II superconductor [1]. (b) Magnetic field line geometry for the corresponding states.

The other important parameter in superconductivity is the coherence length, ξ. This parameter defines the distance over which the wave function of the charge carriers is coherent. For type I superconductors ξ >> λ. In this case the London equations govern the electric and magnetic fields and relate them to currents in the superconductor [1]:

$$\vec{E} = \frac{\partial}{\partial t}\left(\Lambda \vec{J_s}\right) \quad \text{(I.1)}$$

$$\vec{B} = -c\,\nabla \times \left(\Lambda \vec{J_s}\right) \quad \text{(I.2)}$$

where $\Lambda = \frac{4\pi\lambda^2}{c^2}$. Typical values for Nb in this dissertation are ξ = 9.5 nm and λ = 156 nm [18].

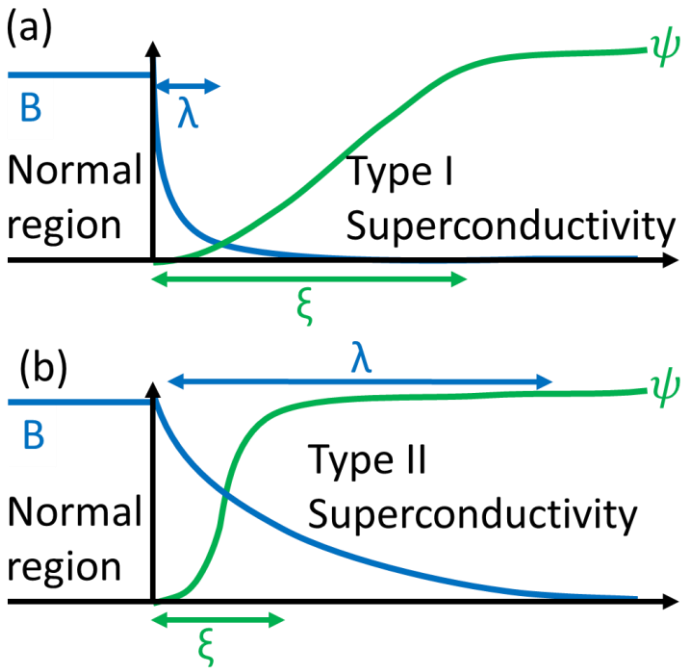

Figure 2. Local magnetic field, B, and charge carrier wave function, ψ, at the boundary between a superconducting surface and a normal region [1] for (a) type I and (b) type II superconductivity.

When a magnetic field is applied to a superconductor, the superconducting-normal state boundary contains a region where the magnetic field has decayed to zero but the superconducting order parameter has not reached its bulk value. This region has a length of approximately (ξ – λ) and increases the free energy of the

system (Figure 2a). This means surface areas in a type I superconductor are minimized in order to decrease the free energy.

In a type II superconductor $\xi << \lambda$. The overlap of penetrating magnetic field with a large superconducting order parameter decreases the free energy of the system (Figure 2b). In order to minimize the free energy, the surface area between normal and superconducting areas must be maximized. Due to the quantization of magnetic flux, the maximum surface area condition occurs when normal regions penetrate the bulk of the superconductor. Each penetrating area contains one flux quantum,

$$\phi_0 = \frac{h}{2e} = 20.7 \text{ Gauss } \mu m^2, \quad \text{(I.3)}$$

where h is Planck's constant and e is the charge of an electron [19]. These flux quanta are surrounded by a current vortex that shields the rest of the superconductor from the flux. Consequently, there can be a coexistence of flux penetration and superconductivity in a type II superconductor.

At low fields and temperatures, flux cannot enter the superconductor [20]. This state is called the Meissner state and is completely diamagnetic. Once a critical field, H_{C1}, is reached, the superconductor allows flux to penetrate (Figure 1). If the superconductor is exposed to the second critical field, H_{C2}, it becomes normal. In bulk superconductivity a surface super-current can persist until H_{C3}, at which point the surface stops being superconducting.

When the thickness of the superconductor is greater than the penetration depth, the normal regions consist of tubes of flux penetrating from one edge of the superconductor to the other. These flux tubes are oriented approximately parallel to the direction of the applied magnetic field (the flux tubes can twist around each other and move within the superconductor). This dissertation focuses on thin film superconductors where the thickness of the film is comparable in size to the magnetic penetration depth. This causes the flux packets to exist as thin, two-dimensional vortices.

I.2.2 Superconducting vortices

Due to the flux quantization condition the number of vortices in a superconductor is proportional to the applied magnetic field. Because the free energy of the superconducting-normal boundary is negative, two vortices close together will repel each other. In a very clean superconductor under these conditions the vortices arrange themselves into a regular close packed lattice [21]. The lowest energy state, the Abrikosov lattice, is a triangular lattice where each vortex has six nearest neighbors (Figure 3a). A slightly higher energy configuration, although still encountered at low energies when in the presence of a pinning potential, is the square lattice (Figure 3b).

Since the number of vortices in the superconductor is proportional to the magnetic field, the number of vortices per unit area, n, can be calculated (in SI units):

$$B = \phi_0 n \tag{I.4}$$

where $B = \mu_0 H$ is the applied magnetic field (μ_0 is the permeability of free space). Using this formula the lattice parameter for different lattices can also be calculated:

$$a = \left(\frac{1}{\sin 60°}\frac{\phi_0}{B}\right)^{1/2} = 1.075\left(\frac{\phi_0}{B}\right)^{1/2} \quad \text{(Triangular)} \tag{I.5}$$

$$a = \left(\frac{\phi_0}{B}\right)^{1/2} \quad \text{(Square)}. \tag{I.6}$$

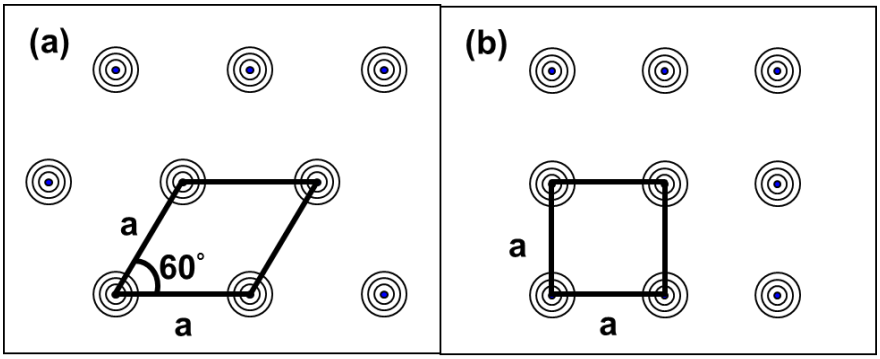

Figure 3. Vortex lattice configurations for (a) a triangular lattice and (b) a square lattice. In both figures a black outline surrounds the unit cell.

Due to the magnetic nature of a vortex, the lattice also interacts with any free currents in the system through the Lorentz force:

$$\vec{F} = \vec{J} \times (\phi_0 \hat{z}) \tag{I.7}$$

where $\vec{F}$ is the force per unit length on a vortex (the thicker the film the higher the force), $\vec{J}$ is the current density, and $\hat{z}$ is a unit vector pointing perpendicular to the film in the direction of the magnetic field of the vortex. Consequently, the vortices feel a force perpendicular to the current direction. If the vortices begin to move due

to this force, the Lorenz transformations of electromagnetic fields dictate that the moving B-field creates an electric field (in the classical limit):

$$\vec{\boldsymbol{E}} = \vec{\boldsymbol{B}} \times \vec{\boldsymbol{v}}. \tag{I.8}$$

Solving these equation yields that the electric field, $\vec{\mathrm{E}}$, is in the same direction as the current density, $\vec{\mathrm{J}}$. This is the condition for Ohm's law. The superconductor therefore has resistance, and the motion of vortices is dissipative.

At steady state the dissipation requires that the velocity of the vortices be proportional to the force. The assumption that the vortices are moving at a constant velocity rather than accelerating and decelerating is used frequently when simulating the lattice to reduce computation time [22]. Under the assumption that the vortices are moving with a constant velocity, we can approximate the speed of the vortices. For a typical 50 μm X 50 μm sample, resistance at the temperatures used in the measurements is on the order of 10^{-2} Ohm. Electric currents up to 100 μA can be applied and typical fields used in this dissertation are on the order of 10^{-2} Tesla. Using equation (I.8) yields a vortex velocity of approximately 1 m/s. For feature sizes under 1 μm this means the relevant time scales are on the order of microseconds. The transport measurements in this dissertation are performed at frequencies under 50 kHz. This time scale is much longer than the time scale of the individual vortex dynamics so we do not expect any time dependent effects.

I.2.3 Vortex pinning

Resistive dissipation causes a variety of problems in superconductor based technologies. In superconducting transmission lines the dissipation causes a reduction in the efficiency [12,13]. Dissipation also reduces the coherence times in superconductors when using them for quantum computation. In addition, vortices are responsible for noise in a variety of superconductivity based devices [14]. Pinning the vortices can reduce these effects.

At low temperatures and currents there is an intrinsic pinning of the vortices from inhomogeneities in the material such as grain boundaries, dislocations, and rough surfaces [13]. This pinning locks the vortices in place and reduces the resistance. The intrinsic pinning of the flux lines is also responsible for the suspension of superconductors in magnetic fields [15]. It is possible however to create artificial pinning sites. Nanolithography enables positioning pinning structures at length scales similar to the vortex interaction length in superconductors. This provides the means to manipulate the potential-energy landscape. For instance, square and triangular pinning arrays substantially increase the critical current at magnetic fields corresponding to integer ratios between the density of vortices and the pinning sites [23]. This effect is pronounced in transport measurements where the resistance decreases by several orders of magnitude at specific magnetic fields [24]. These are known as the matching minima because they occur at the fields where the vortex lattice density matches the pinning lattice density. Rectangular [25,26], kagome [27],

honeycomb [28], and quasiperiodic arrays such as the Penrose lattice [29,30], Fibonacci series, and fractal structures [31] show more complex matching minima structures due to the interplay between the array symmetries and the vortex lattice.

The size and the magnetic state of the pinning sites has also been measured [32]. It was found that increasing the size of the pinning sites did not have a large effect on the pinning. However, if the separation between the pinning sites became too small the system transitioned into a superconducting wire network state and Little-Parks oscillations could be seen [18]. Measurements of the magnetization showed that pinning sites in the magnetic vortex state produced much higher pinning [33]. This is due to increased stray fields in the center of the magnetic vortex. For this reason, the transport measurements in this dissertation used magnetic dots to pin the vortices. In order to enhance the pinning effects, the pinning sites were placed under the superconducting film so that the corrugation of the film could also contribute to the pinning.

I.3 Nanofabrication techniques

I.3.1 Electron beam lithography

The placement of the pinning sites is crucial to control the energy landscape of the vortices. Electron beam (e-beam) lithography allows the exact control of an array of pinning sites with a precision of a few nanometers. The position and shape of

each pinning site can be programmed into an e-beam lithography system to tailor the nanostructures to the designated specifications (Figure 4).

To make a pinning array a silicon substrate has a layer of Polymethyl methacrylate (C4-950PMMA Resist) spun on top at 5000 RPM for one minute. The substrate is baked for 5 minutes at 195 °C. It is then placed inside a Jeol JSM 6400 scanning electron microscope that has been converted to an electron beam writer using the nano pattern generation system (NPGS). The pinning pattern is written into the resist with a pixel size of 20 nm X 20 nm and a dose of between 1 and 6 femto Coulombs/pixel. The actual exposure current used is typically between 30 and 50 pico Ampere.

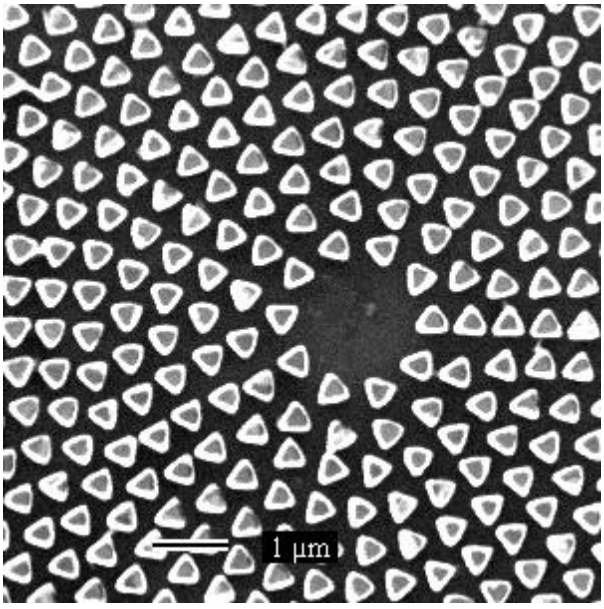

Figure 4. An array of pinning sites made with electron beam lithography. Here the pinning sites are arranged in concentric circles. The pinning sites themselves have a triangular shape.

Once the pattern is written into the resist, the sample is developed in 1 part methyl isobutyl ketone (MIBK) and 3 parts Isopropanol for 15 seconds. The sample is rinsed in Isopropanol to stop the developing and then dried with N_2 gas. Once a material is deposited on the sample, liftoff is performed in acetone for approximately 12 hours followed by low power sonication for five seconds. The sample is rinsed again in isopropanol, washed in de-Ionized water, and dried with N_2 gas.

I.3.2 Porous alumina masks

Typically, an array of pinning sites 1 mm X 1 mm in area can take up to five hours to pattern using electron beam writing. Larger areas become prohibitively expensive and time consuming to produce. Additionally, if the area is large, the bending of the electron beam at the edges can cause asymmetries in the pattern between different points. This problem can be avoided if smaller write-field areas are chosen but then there are stitching errors when attempting to put two write-fields together. The porous alumina fabrication technique allows the fabrication of large ordered arrays of pinning sites [34]. Using this technique an array of pinning sites 70 nm in diameter and 100 nm in spacing can be fabricated over a 1 cm X 1 cm area in a couple of days (compared to a continuous 500 hour e-beam writing session).

For the porous alumina mask, a 2 μm thick film of aluminum is grown on a silicon substrate using e-beam evaporation. The aluminum is then anodized in Oxalic acid. The application of a voltage leads to the formation of an oxide surface, while pores in this surface arrange into a self-assembled triangular lattice [35]. The

Aluminum is anodized until the pores are approximately 1.7 μm in depth and then the oxide is removed using a solution of chromic and phosphoric acid. This number is chosen so that approximately 300 nm of material is left to increase the success probability of the liftoff. The process is repeated in a second anodization. The first anodization provides a seed for the positions of the pores so that during the second anodization the order of the pores is increased [36].

Once the bottom of the pores reaches the substrate, we can deposit material into the 300 nm deep pores. It is important that when the deposition is performed, very little material is deposited on the edges of the pores, otherwise liftoff is usually unsuccessful. Sputtering and chemical vapor deposition techniques are not favored for this reason. Once the material is deposited, the aluminum oxide lift-off can be performed in a solution of chromic and phosphoric acids leaving the dot array on the silicon sample.

I.3.3 Photolithography

For large areas with custom features UV lithography works well. Using a Karl Suss MJB 3 mask aligner, feature sizes as low as 2 μm can be achieved and the size of the exposed area can have a diameter of over 2 inches. These features make UV lithography an ideal method for placing contacts and other large structures on a pinning pattern.

Two resists were used for photolithography: Microposit S1818, a positive resist, and Futurrex NR9-1500PY, a negative resist. By switching between positive and

negative resists, a liftoff process versus an etching process can be tested using the same pattern on the mask. The S1818 was spun on the sample at 5000 RPM for one minute and then baked at 115 °C for one minute. The resist was exposed to UV light for 2.5 minutes at an exposure power of 0.4 mW/cm^2. After exposure it was placed in 1 part deionized water and 1 part Micro-developer (now called AZ developer) for approximately 40 s using visual checks to confirm the resist developed properly. After being washed in water, the next fabrication step could be performed on the sample. Once the sample was ready, the resist could be removed in Acetone. It is important to note that once etched, S1818 can become very difficult to remove. One method to overcome this problem is to use an O_2 plasma etch to remove the resist. There are other wet etches that can be used but the solutions were not found to be very effective.

When using NR9-1500PY resist, the resist was spun on the sample at 5000 RPM for 40 s. It was then baked at 150 °C for one minute. The exposure was performed for 3 minutes at a power of 0.4 mW/cm^2. Once exposed the sample was baked again at 100 °C for one minute and then developed for 8-12 s in pure RD-6 resist developer while agitating the sample. The sample was then immersed in deionized water and agitated for approximately 10 s, followed by flowing water over the sample for another 10 s. This process ensures no resist particulates were left on the sample after development. Once processed the resist was removed by immersion

in acetone for no fewer than 4 hours. It was then sonicated at low power for 5 s, rinsed in Isopropanol and then deionized water.

When using the NR9-1500PY for small feature sizes (approximately 2 μm), the mask was sonicated first for 5 minutes in Acetone, Methanol, and Isopropanol. The mask was then rinsed in deionized water and baked at 100 °C for 5 minutes. Once allowed to cool for 10 minutes the mask could be used for photolithography. If this process was not completed the features became spread out and merged with other features.

I.3.4 Etching

Etching was employed in the fabrication of linear devices (non-Corbino geometry) when making the contacts. The Corbino geometry, requiring stacked layers, employed a liftoff only fabrication to ensure no resist was left on the substrate. The benefit of plasma etching is that reactive gases can etch selectively and quickly. For example, to etch Nb, 30 mBar of CCl_3F was used with a very small amount of O_2 at 50 W of power. The etch rate was approximately 20 nm/minute. Using non-reactive etching is much slower but can etch away most materials on a substrate. 20 mbar of Ar at 70 W allowed the etching of Nb at a rate of approximately 2.5 nm/minute. After an Ar etch, a plasma with pressure 30 mbar O_2 and 70 W power for 30 minutes was employed to remove the resist.

I.3.5 Film growth

Two main methods of film growth were used for this dissertation, AC sputtering and electron beam evaporation. The sputtering system (Microscience) operates at a base pressure of 10^{-7} Torr. One of the important parameters to remember in sputtering is that at 10 mTorr, a particle that has moved 10 cm has had an average of 10 collisions along the path [37], meaning the particles are no longer ballistic and are now moving in random directions. Consequently sputtering systems can deposit material on all surfaces of the sample, including the walls of the resist. This can produce fences during liftoff processes – thicker material areas on the boundaries of features.

For electron beam evaporation a Kurt J. Lesker (KJL) system was used with a base pressure of 5 X 10^{-7} Torr. For very high powers and low pressures, a RIBER molecular beam epitaxy (MBE) system with a base pressure of 10^{-10} torr was used. Since materials in electron beam evaporation move ballistically, resists with undercuts (Figure 5) allow material to be placed on the substrate without hitting the edges, improving the definition of the features.

For the Co and V pinning sites both deposition methods were used. When sputtering, the Ar gas was flowed through the chamber and pressure was maintained at 4 mTorr while 100 W of power was applied to the target. In the electron beam evaporator, the power was chosen to maintain a 0.5 Å/s rate.

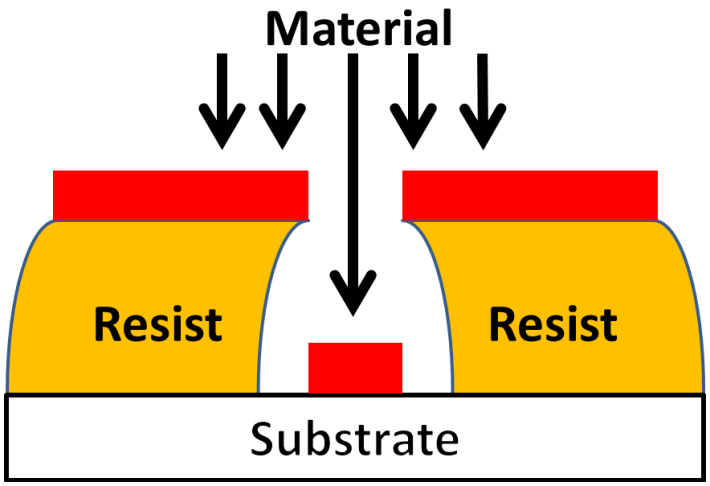

Figure 5. Ideal deposition conditions include resist with an undercut in order to prevent material from climbing up the resist edges.

When depositing Al for the porous alumina samples a rate of 2.0 Å/s was maintained in the KJL evaporator. The KJL evaporator was also used for Au with a rate of 1.0 Å/s. In order to ensure other layers adhered to the Au a 100 Å layer of Ti was deposited at 0.3 Å/s on top of the Au. SiO_2 was also grown in the chamber with a rate of 1.0 Å/s. A systematic study of the SiO_2 was performed and it was shown that for an area of approximately 1 mm X 1 mm, the SiO_2 did not provide a resistive layer if it was thinner than 600 Å or thicker than 900 Å. This is probably due to pinholes and peeling.

Nb was grown using sputtering and electron beam evaporation in the MBE. It was sputtered at 4 mTorr with 100 W applied to the target. It is important to pre-sputter the target for 5-10 minutes before use, especially if the chamber has been recently opened. When using the MBE the sample holder was kept at 25 °C and a

rate of 3 Å/s was maintained. The large rate was to ensure the purity of the Nb on the sample because the superconducting T_C of the Nb is very sensitive to magnetic impurities. The MBE produced Nb with a T_C of 9.2 K consistently. The sputtering system produced T_Cs between 5 and 8 K, however as the system was used more frequently, T_Cs of 8 K became more common. This is probably due to etching of the sputtering target and conditioning of the chamber.

I.4 Measurement

The transport measurements were performed in a Janis liquid He (LHe) cryostat. It has two vacuum jackets. The first jacket separates the liquid N_2 space from the air and the LHe reservoir. The second vacuum jacket separates the LHe reservoir from the sample space. The two spaces are connected through a needle valve, which allows a small flow of LHe into the sample space to cool it down. In order to precisely control the temperature, there are two temperature sensors and heaters controlled by a Lakeshore 332 temperature controller, one close to the needle valve and one on the sample holder. By having a very small LHe flow, and a heater with proportional-integral-derivative (PID) controller values where the proportional value is very low, the integral is very high and the derivative is zero, a temperature stability of ±20 mK can be maintained at the needle valve sensor. This is crucial to maintaining a ±1 mK stability on the sample. It is important to note that occasionally the resistance would show noise due to temperature instability even though the temperature controller (precise to 1 mK) did not. This is because a typical

superconducting transition changes more than 3 orders of magnitude in resistance over a temperature range of approximately 0.2 K. With this setup, samples can be measured at temperatures ranging between 1.8 K (when pumping on the sample space) and 300K.

The magnet in the cryostat can reach 7 Tesla, or 9 Tesla with the lambda point refrigerator. It uses a persistent current heater to reduce He consumption when maintaining high fields. The magnet is controlled with a Cryomagnetics Inc. 4G superconducting magnet power supply. The power supply allows a precision of ±1 Gauss, although a small drift of the magnetic field has been observed over a period of 5 minutes without a corresponding change in the displayed field. For the experiments in Chapter II, a Cryomagnetics Inc. CS-4 power supply was used.

The sample was connected to the sample holder using either double sided tape for quick measurements or GE varnish for better heat conductivity. Indium solder was used to connect the contacts to the sample holder and Teflon tape was wrapped around the wires as a strain relief. The wires were connected to a switch box, which could be connected to a Keithley 6220 precision current source and Keithley 2182A nanovoltmeter. These two instruments can be connected to each other and measurements can be performed using the standard dc polarity reversal mode [38]. In this mode a low frequency (on the order of a few hertz) square wave current is passed through the sample and the voltmeter is triggered and read

automatically for the high and low current values. In this way, the voltage offset can be averaged out and more accurate readings can be taken.

CHAPTER II

THE ROLE OF DISORDER IN THE PINNING LATTICE

II.1 Introduction

Disorder is the origin of many effects such as the low temperature resistance of metals [39], melting transitions, and the transition from ferromagnetic order to paramagnetic order. It can be engineered into systems to produce different types of ordering, for example antiferromagnetic to ferromagnetic ordering [40], and spin glass [41]. While the study of these systems is prevalent throughout condensed matter, there has been little research reported in the literature dealing with disorder in superconducting vortex physics.

There are application based reasons to study disorder in superconducting vortex physics as well. One of the main goals for studying vortex pinning has been to use periodic arrays to enhance the critical currents in superconductors [42]. However, extending periodic lattices to macroscopic sizes introduces disorder. For example, one of the most promising methods of creating macroscopic sized arrays, self-assembled systems like porous alumina, introduces defects into the lattice [43]. Even electron beam lithography introduces stitching errors when trying to make very large areas. It is important to study and recognize the effects of disorder if we're going to apply the knowledge we've learned from ordered pinning arrays to macroscopic systems.

A completely disordered array will not show matching effects [29]. It will however, still increase the critical current of a system due to partial vortex pinning [44]. In contrast, completely ordered arrays show a pronounced enhancement of the critical current at well-defined matching fields [42]. Quasi-periodic arrays have also been studied and the periodicities in the lattice can be extracted from the matching fields [29–31]. There have been a few studies focusing on the effects of disorder including some that preserved long range periodicity [45,46], and others that studied disorder caused by self-assembled arrays of pinning sites [47,48]. In this chapter we study the effects of disorder in the pinning lattice on the vortex flow by varying both the type of disorder and the amounts of disorder for different samples.

II.2 Experiment

II.2.1 Choosing the right disorder

Several methods were considered to introduce disorder into the pinning lattice. In ref. [45] the authors studied disorder with long range periodicity by taking an ordered lattice and moving each pinning site a random distance away from its original lattice point. In this algorithm, disorder in the lattice is created but periodicity still exists on the large scale. The results show a decrease in pinning, especially at the higher order matching fields.

Another possible method is to dilute a pinning lattice. In this method random pinning sites are removed from an ordered lattice so that there is still long range periodicity, but on the short range the random pinning sites that were removed disrupt the order. In this case, the dilution percent of the lattice is the order parameter. One problem with this method is that the density of the pinning sites changes as the dilution is varied, which adds complications to the interpretation of the results. The dilution type of disorder is studied for several different dilutions and lattice types in section II.4.

Self-assembled structures naturally exhibit disorder [49,50]. There are many dislocations in self-assembled structures and it is important to understand how these dislocations affect the vortices. A drawback for using this method to introduce disorder into the lattice is the difficulty in controlling the precise amount of disorder present in the pinning array. For example in porous alumina one way to introduce disorder is by limiting the number of secondary anodizations after the first, preventing the self-assembly process from reaching the ordered configuration (see I.3.2 Porous alumina masks). However, this only gives a rough control, and furthermore it is difficult to keep the shape of the pores uniform. Still, this method is useful if one wishes to do measurements on large arrays of disordered pinning sites. In section V.2.2 a project is discussed that will measure vortex pinning in disordered porous alumina systems using microwaves to perform magnetic susceptibility measurements [51].

The system we chose to study creates disordered arrays of pinning sites using the two dimensional "parking" algorithm [52]. This algorithm can easily be transferred into an e-beam lithography pattern, it gives us order with a controllable range, and it can provide us with a constant density of pinning sites.

II.2.2 The two dimensional "parking" algorithm

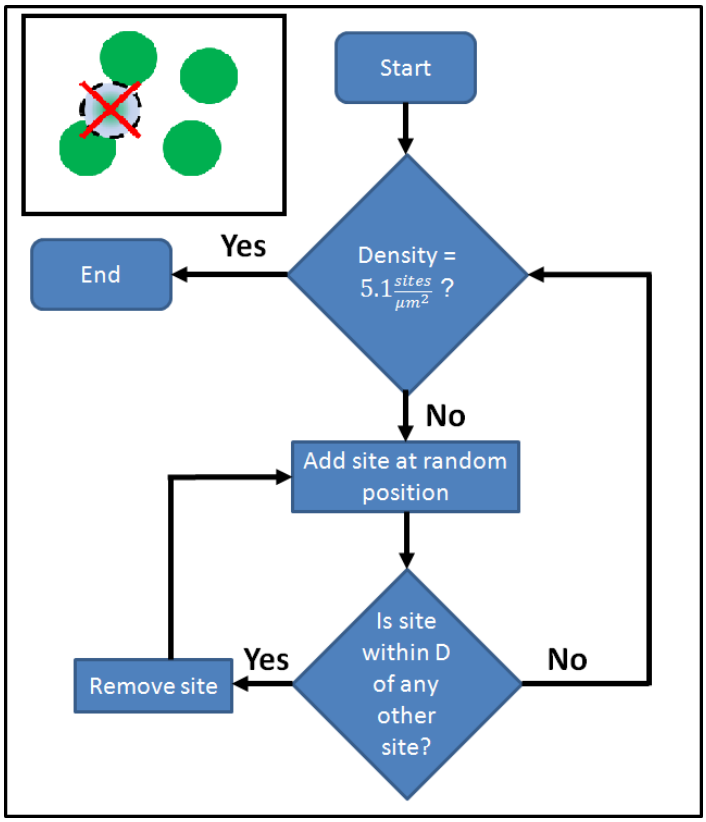

Figure 6. Flow chart describing the "parking" algorithm used to generate disorder. D, the hard circle diameter, is the order parameter for this algorithm. The inset at the top left shows a hard circle that follows the 'Remove site' branch of the chart.

The two dimensional "parking" algorithm (Figure 6) uses hard circles (as opposed to hard spheres for the three dimensional version) with a constant

diameter. The diameter chosen for the hard circle is the order parameter of the algorithm and is not related to the diameter of the pinning sites. The circles are randomly placed in a given area. As they are placed, each circle is tested for overlap. If there is overlap with any previously placed circles, a different position is chosen. This algorithm allows us to keep adding circles in order to obtain the specified density for the chosen area. It also allows us to control the order in the system by modifying the diameter of the hard circle. If a short order is required, the hard circle diameter is chosen to be small so that the circles can get closer to each other. This leaves gaps elsewhere and causes clusters of dots to appear in randomly placed configurations (Figure 7a). It is also closer to the completely disordered case where there are no interactions between the placements of the different circles.

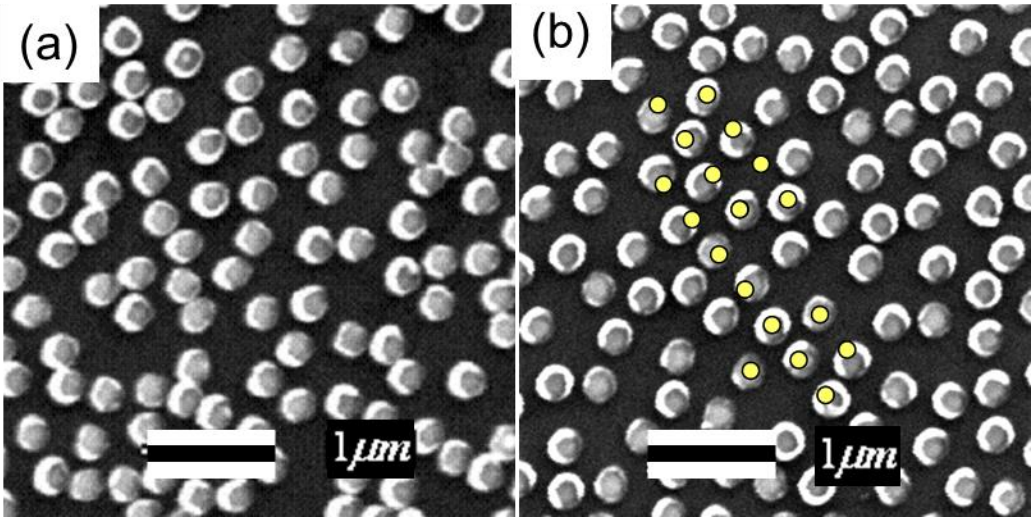

Figure 7. Pinning sites created with different order parameters. (a) A diameter of D = 280 nm and a more disordered array. (b) A diameter of D = 370 nm. Yellow dots on the figure have been placed as a guide to the eye to illustrate order in the lattice. Reprinted from Y. J. Rosen *et al*., Phys. Rev B 82, 014509 (2010). Copyright by the American Physical Society.

Similarly, to generate order with a longer range we increase the hard circle diameter (Figure 7b). In this situation dots can only be placed in certain positions. Empty space is used up, and the lattice approaches the ordered triangular lattice – the lattice that has the largest hard circle diameter. The two dimensional "parking" algorithm does have limitations however in that there is a maximum allowable hard circle diameter that can be used. This limit does not allow us to reach the triangular lattice. In the case of the chosen density ($5.1/\mu m^2$) the maximum hard circle diameter is D = 370 nm [53], compared to the triangular lattice spacing of 480 nm. The existence of an upper limit is due to the statistical impossibility of placing every pinning site in the triangular lattice (for the second lattice point there were $2x10^4$ triangular lattice positions out of a possible $2^{53} \approx 10^{16}$ positions for the precision used when implementing the algorithm).

There is also a lower limit for the hard circle diameter due to the fabrication process. Since the pinning centers have a finite size, too small a diameter will cause them to overlap. In our implementation the lowest diameter used was D = 225 nm.

We used the pair correlation function (PCF) to characterize the disorder. The PCF is commonly used to analyze liquids and other disordered system. It quantifies the normalized density for a system as a function of the distance, r, away from an average particle. In the case of a square or triangular lattice this would mean delta function peaks at the nearest neighbor distance, the second nearest neighbor distance, etc. However, in the case of a liquid, large peaks appear close to the

particle's diameter. At distance much larger than that diameter the sample becomes disordered and the PCF becomes one.

The following equation is used to calculate the PCF [54]:

$$PCF(r) = \frac{1}{N_T} \sum_i \frac{1}{\rho} \frac{N_i(r \to r + \delta r)}{2\pi r \, \delta r} \qquad \text{(II.1)}$$

where N_i is the number of sites contained in a ring centered at the ith site. The ring has radius r and width δr. By dividing the number of sites by the area of the ring ($2\pi r \, \delta r$), the density of sites in that shell is obtained. The result is then normalized by the density, ρ. Finally the results are summed over all sites and normalized again by the total number of sites used in the calculation, N_T. The resulting PCF gives a measure of the probability of finding a site a distance r away from any other site.

Figure 8 shows the PCF as a function of distance for the four disordered samples. The vertical lines are the PCF for a triangular lattice, in this case delta function peaks at the nearest neighbor positions. The dashed horizontal line on the graph is the PCF for a completely disordered system. The graph shows that for D = 370 nm there is a large peak at the hard circle diameter. There are then several oscillations, after which the PCF settles to one at about 1100 nm. The point at which the PCF settles to one and becomes disordered is called the "range of local order" (RLO) [55]. This number is used to compare the length scale of the order between samples. In contrast to the most ordered sample, the least ordered sample, made

with D = 225 nm, has an RLO of approximately 400 nm. This value is below the nearest neighbor distance for a triangular lattice with the same density.

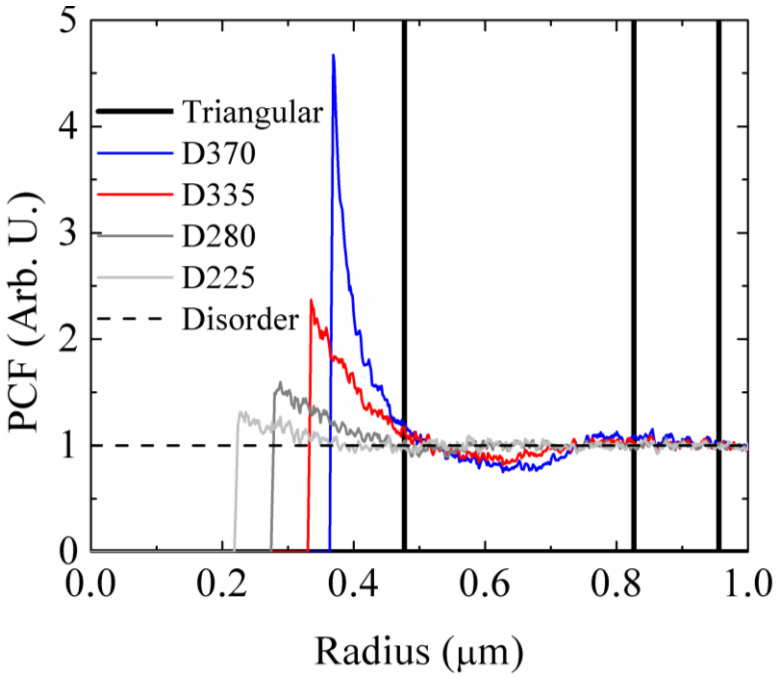

Figure 8. Pair correlation functions (PCF) for the four fabricated samples. The black vertical lines represent the pair correlation for a triangular lattice. The dashed horizontal line is the pair correlation for a completely disordered system. Reprinted from Y. J. Rosen *et al*., Phys. Rev B 82, 014509 (2010). Copyright by the American Physical Society.

II.2.3 Sample fabrication and measurement techniques

The samples were fabricated on Si substrates using a conventional lift-off technique combined with sputtering. The pinning sites were written in polymethyl methacrylate using standard e-beam lithography. Cobalt dots (250 nm diameter and 40 nm thick) were prepared using standard AC sputtering and liftoff. To complete the structure, a 100 nm thick layer of Nb was evaporated on top of the dots, and then photolithographically patterned to a 50 X 50 μm^2 resistance bridge.

Magnetoresistance measurements were conducted in a variable temperature liquid-He flow cryostat with temperature stability better than 1 mK. The resistance was measured using a current source and nanovoltmeter in standard dc polarity reversal mode [38]. Each sample was measured at four different temperatures ranging from T/Tc=0.96 to 0.99. For each temperature several different R vs. H curves were obtained with current densities between 0.2–20 kA/cm^2. Typically the Nb had a Tc of 9.0 K and a transition width of 0.2 K. Tc is defined as the temperature at which the resistance is equal to 90% of the normal resistance.

Table 1. Sample parameters. The sample designation, the hard circle diameter used to construct the disorder, the derived range of local order, and the value of the first matching field are presented in this table. Note that the range of local order for a triangular lattice is theoretically infinite. The error of the matching field position is the standard deviation from eight measurements performed on the sample at different currents. Reprinted from Y. J. Rosen *et al*., Phys. Rev B 82, 014509 (2010). Copyright by the American Physical Society.

Sample No.	Minimum distance (nm)	RLO (nm)	Center of first matching minimum (B/B_1)
Triangle	480 ± 5	Sample size	1.01 ± 0.02
D=370nm	370 ± 5	1120 ± 10	1.02 ± 0.03
D=335nm	335 ± 5	950 ± 10	0.93 ± 0.02
D=280nm	280 ± 5	630 ± 10	0.86 ± 0.02
D=225nm	225 ± 5	410 ± 10	0.80 ± 0.06

Five samples (see Table 1) with different degrees of order were investigated. For comparison we measured a sample with a regular triangular array and a lattice spacing of 480 nm. The other four samples have decreasing degrees of order, generated using D = 370, 335, 280, and 225 nm, all with the same average density as

the triangular lattice. D = 370 nm is the most ordered realization the algorithm can produce for this density [53] and for D = 225 nm the Co pinning centers start to overlap.

II.3 Results and discussion

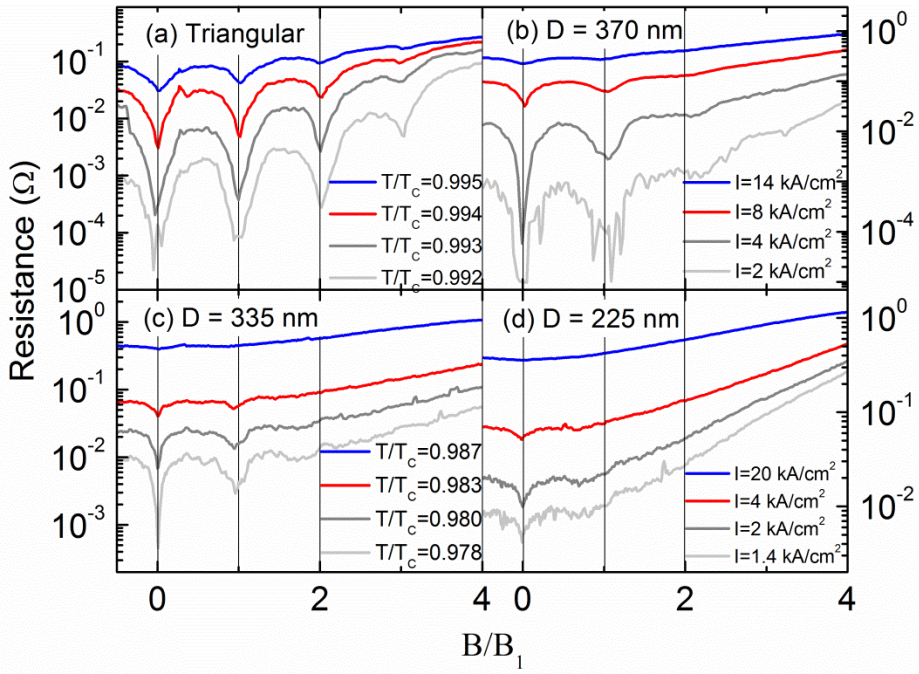

Figure 9. Magnetoresistance as a function of field for the different samples. (a) Triangular lattice and (c) D = 335 nm samples at a constant current density of I = 2.0 kA/cm^2 and several different temperatures. (b) Sample D = 370 nm, the least disordered sample, at constant T/Tc = 0.973 with varying currents. (d) Sample D = 225 nm, the most disordered sample, at a constant T/Tc = 0.972 with varying currents. Vertical lines at the matching fields are added as a guide to the eye. The curves have been shifted for clarity. Reprinted from Y. J. Rosen *et al.*, Phys. Rev B 82, 014509 (2010). Copyright by the American Physical Society.

Figure 9 shows the magnetoresistance of samples with different degrees of order at currents and temperatures which display the most pronounced matching minima for each sample. The superconducting transition widths of the disordered

samples were approximately double the transition width of the triangular sample. It is therefore difficult to compare the triangular sample to disordered samples at similar values of T/Tc's. The magnetic field was normalized to the first integer matching minimum of the triangular lattice, $B_1 = \beta\Phi_0$, where $\Phi_0 = 20.7G\mu m^2$ is the flux quantum and β is the pinning-site density [23,56].

The magnetoresistance minima indicate matching effects between the vortex lattice and the pinning sites [24]. The locations of matching minima are not affected by temperature (Figure 9a and c) or current (Figure 9b and d) in any of the samples. The matching minima of the triangular pinning-site lattice are shown in Figure 9a for different temperatures and a current density of 2 kA/cm^2. Three matching minima appear at the expected magnetic fields as predicted by the pinning-site density. The magnetoresistance of sample D = 370 nm (Figure 9b) also exhibits a first matching minimum as expected from the pinning-site density. However, the high-field features are different from those of the triangular lattice, in spite of the fact that this is the most ordered sample. The second matching minimum is barely observable, not located at an integer multiple of B_1, and there is no discernible third matching minimum. With decreasing order (Figure 9c and d) the matching minima become wider and shallower. However, matching minima appear even for the most disordered sample D = 225 nm. To emphasize the less pronounced features we show in Figure 10a representative magnetoresistance curves for each sample, in which the background resistance was subtracted. Matching minima can be resolved for all

degrees of disorder. For example, even sample D = 225 nm (most disordered, top light gray curve) shows a wide minimum centered on 0.8 B_1.

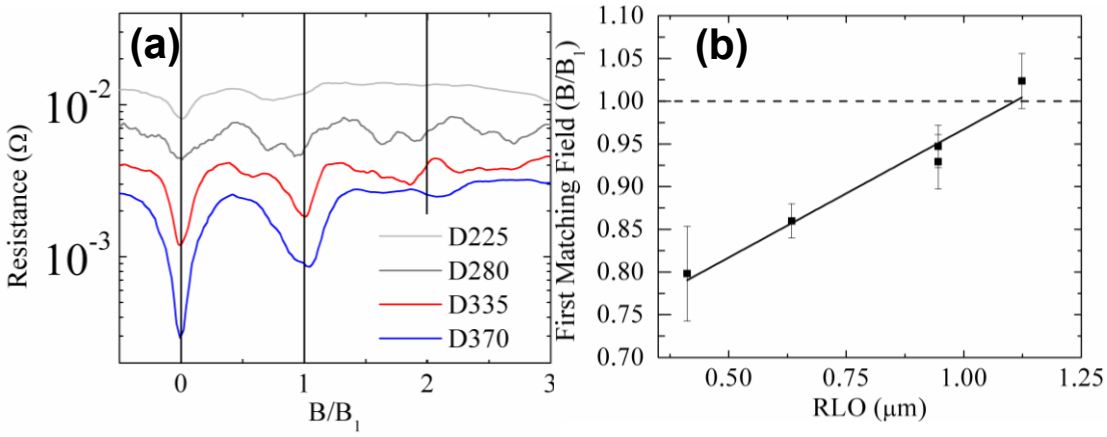

Figure 10. (a) Magnetoresistance as a function of field for the different samples with backgrounds subtracted and heights shifted for clarity. (b) The position of the first matching minimum for different samples plotted against the RLO. The error bars are due to noise in the PCF which makes it difficult to determine the exact RLO. The dotted line is the theoretical first minimum position of a triangular lattice. Reprinted from Y. J. Rosen *et al.*, Phys. Rev. B 82, 014509 (2010). Copyright by the American Physical Society.

Surprisingly, Figure 10a show the first minimum shifting toward lower fields with decreasing order. Figure 10b shows the positions of the first matching minima averaged over eight measurements versus the RLO. The location of the first matching minimum increases in field linearly with the RLO and reaches the value of the triangular lattice at D = 370 nm. For all disordered samples there are additional magnetoresistance features at higher fields (Figure 10a), which were reproduced at different temperatures and currents, ruling out experimental artifacts. The features appear as smaller peaks and valleys with their position changing from sample to sample, indicating complex sample-specific matching effects. For example, in sample

D=280 nm (dark gray curve, second from the top in Figure 10a) there is one minimum at a value slightly less than $B/B_1 = 1$, and two small minima at B/B_1=1.6 and 2.5. The first minimum is in the vicinity of the first matching field, but the additional features are far from the other expected matching fields.

Measurements of systems without ordered pinning centers do not show matching minima [29]. We find however, that the least ordered sample does contain matching minima even though the RLO is shorter than the lattice constant of a triangular array with the same pinning density. Our results indicate that any amount of order, defined as a non-unity PCF, correlates with enhanced pinning of the vortex lattice. Accordingly, one would expect the matching minima to occur at vortex densities related to the length scale for which the PCF has a maximum. Since the PCF maximum decreases with decreasing order (Figure 8), this should result in the matching minima appearing at higher densities, and therefore larger fields. Surprisingly, our results (Figure 10a) indicate the opposite. Decreasing the order leads to smaller fields for the first matching minimum. Interestingly, we find a linear correlation of the RLO with the first matching minima positions (Figure 10b). A lower RLO means there is less long-range order. The vortex lattice, which energetically prefers long range order, must deform in order to pin to the pinning sites. This causes the vortices to be in a less stable pinning configuration which would explain why the matching minima become shallow. We can account for the magnetoresistance minima shifting to a lower field in the following way. At all distances shorter than the

RLO the pinning sites contain a certain degree of order. The vortex-vortex interaction is repulsive (decaying approximately exponentially as a function of R/λ [57], where R is the vortex-vortex distance and λ is the magnetic field penetration depth). This means that at lower vortex densities, and therefore larger average vortex-vortex distances, the force on each vortex is smaller, allowing it to relax and pin better to the less ordered pinning lattice. Thus, the best vortex lattice pinning (the minima in the magnetoresistance) will occur at the lowest vortex density for which there still is long-range order, and this is the RLO.

The high-field landscape of the magnetoresistance is very interesting and different from that found in disordered, quasiperiodic, or vacancy potentials [58]. In a quasiperiodic potential, at high magnetic fields the elastic energy of the vortex lattice is large and overcomes the pinning [31]. In a triangular lattice with vacancies there were no indications of complex high-field vortex lattice pinning [58]. In the two dimensional “parking” algorithm we find that at higher fields there are additional shallow minima that do not relate to the integer matching fields. These features are reproducible for all temperatures and current densities. The features may be connected to the maximum in the PCF, which occurs at low pinning site separation values. The partial order in the pinning sites at the low separation values, could pin the vortex lattice when it is at higher densities.

It is interesting to note that some of the small features appear to be related to each other between some of the samples. For example in Figure 10a sample

D = 280 nm shows two peaks approximately equal in depth, while sample D = 335 nm shows a small peak next to a large one. During the implementation of the disorder algorithm the random seed was kept the same for the different samples. This means that 50-70% of the pinning sites are placed in the same locations for the different samples (depending on the order). Possible correlation between the different samples could be due to this match. It would be interesting to pursue this as a source of further study as it could mean that the initially placed pinning sites, which are more disordered, are the source of the high field magneto-resistance features. This has not however been studied in detail and only verified claims were published.

II.4 Diluted arrays

As mentioned in section II.1, another method for adding disorder to an array is to dilute an ordered lattice by removing pinning sites from it at random. In this way the overall long range periodicity is preserved in the sample but on short length scales the lattice is distorted. If the vortex-vortex interaction is strong in this system, the interaction will always try to keep the vortices in a regular lattice. This would mean the optimal pinning would happen when the density of vortices corresponds to the density of the full lattice, and the dilution would be ignored. If there is very little order in the vortex lattice, the optimal pinning would occur when the density of vortices corresponds to the actual density of pinning sites. The competition between these two scenarios can tell us about the rigidity of the vortex lattice and the propensity to pin to disordered systems.

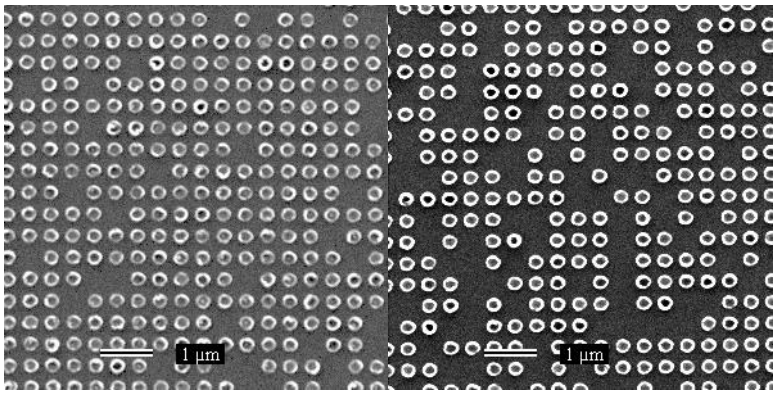

Figure 11. Diluted arrays of dots in square lattices. On the left is a square lattice with 88% of its pinning centers remaining. On the right is a square lattice with 72% pinning sites remaining.

The fabrication was performed in the same way the disordered samples were fabricated. The position of the dots was chosen by creating a square or triangular lattice and randomly removing a percentage of the sites based on the desired density (Figure 11).

Figure 12 shows the first matching field positions (normalized to the first matching field for the undiluted square lattice) as a function of the array density (normalized to the undiluted square lattice). If the matching field positions were a function of only the square lattice parameter it would be at 1.0 regardless of the array density, as shown by the continuous line at the top. However if the vortices do not have a strong vortex-vortex interaction, the optimal pinning should occur when there is one vortex per pinning site, so in other words when the density of vortices is equal to the density of the diluted array. This is represented as a dashed line on the figure.

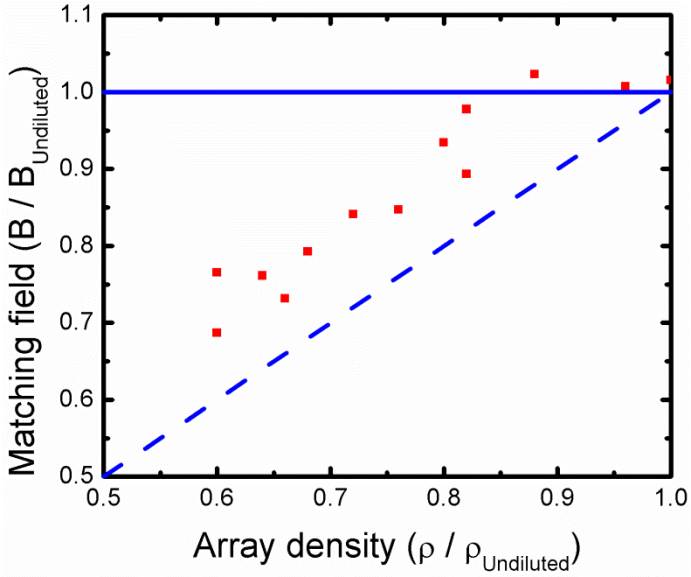

Figure 12. Matching field values of a diluted square array as a function of the array density. The matching fields are normalized to the matching field of an undiluted square lattice. The array density is normalized to the square array density. A vortex lattice matching only to the lattice parameter would follow the straight continuous line on top. A vortex lattice matching only the density of the vortex lattice would follow the dashed line.

The vortices appear to be pinned mostly by the density of the array and not the lattice of the square array. However, there is an offset in the matching, which implies that there is an effect from the square geometry of the pinning lattice. This causes the optimal pinning point to shift to higher fields than it would be if it were just the density of pinning sites that mattered. This is the opposite effect as the one seen in the "parking" algorithm disorder case, where the optimum pinning went to lower fields than the density would suggest. Here the lattice parameter of the pinning sites shifts the optimal pinning to higher fields instead. These effects were

predicted previously by [59] and subsequently observed by [58] before our results were published.

What was not predicted or seen in other papers is another effect in the diluted arrays related to percolation. In ref. [59] the authors predicted in their simulations that matching effects will be seen even with only 10% of the pinning centers remaining in the lattice. In the case of a triangular lattice we could only see matching effects down to 50% density of the triangular lattice. In the case of the square lattice matching fields disappeared at 60% of the lattice. These numbers match the percolation thresholds for these arrays [60]. The percolation threshold is the dilution at which the lattice points begin to form islands and are no longer connected in one large array through nearest neighbors. It is also the point where a path can be found from one side of the sample to the other without intersecting any of the pinning sites.

II.5 Conclusions

In summary, we measured superconducting vortex pinning in a disordered pinning potential with controlled short range order generated using the two dimensional “parking” algorithm. Magnetoresistance minima characteristic of matching effects are observed even for the smallest degree of order. This indicates that even very low pinning-site symmetry is sufficient for enhanced pinning of the vortex lattice at specific matching fields. The most ordered potential generated by the two dimensional “parking” algorithm shows a pronounced first matching

minimum corresponding to the matching minimum of a triangular lattice with the same pinning-site density. Decreasing the order results in the first matching minimum becoming less pronounced, as may be expected, but also in it shifting to lower fields.

We report on the appearance of additional magnetoresistance features at higher fields. These are reproducible for all temperatures and current densities measured, but vary from sample to sample. We attributed these matching minima to complex interstitial vortex pinning arising from the short range order generated by the algorithm.

Further theoretical and numerical analyses are needed to quantitatively understand these phenomena, and we hope that our study will motivate research of vortex dynamics theories in this direction. These must account for the fact that small amounts of order in the pinning sites lead to enhanced pinning at fields lower than the matching fields due to the reduced range of local order.

There was also an increase in the matching field values for a particular density when the array was formed into a regular lattice that was missing pinning sites. There appears to be a threshold to the amount the field can be raised due to the percolation threshold of a diluted array. However, in order to verify the percolation threshold hypothesis investigation of more lattice types is required.

II.6 Acknowledgements

Chapter II, in part has been previously published in: Y. J. Rosen, A. Sharoni, and Ivan K. Schuller, “Enhanced superconducting vortex pinning with disordered nanomagnetic arrays,” Phys. Rev. B 82, 014509 (2010). The dissertation author was the primary investigator and author of this material. Y. J. Rosen selected the experiment and algorithm to use, fabricated the samples, performed the analysis and was the primary author on the paper.

CHAPTER III

RECTIFICATION OF VORTEX MOTION

III.1 Introduction

The equations of motion in physics exhibit time-reversal symmetry. However, many systems such as the biological mechanism responsible for muscle contraction [61], diodes [62], and mechanical ratchets, do not exhibit symmetry in time. Studies of simple systems where time-reversal symmetry is broken can shed light on the mechanisms that cause this irreversibility.

A rectifier is a system that reacts to forces of equal magnitude but opposite in direction with different magnitude responses. When a time symmetric signal (such as a sinusoidal, square, or triangular wave) drives a rectifier, it yields a biased response with a non-zero average value. Rectifier systems commonly arise out of asymmetric potential energy landscapes like the one in Figure 13a. In that type of system, a small force will not be able to ascend the steep potential but may be able to overcome the gradual potential in the opposite direction.

Superconducting vortices with asymmetric potentials are an example of a system that exhibits rectified behavior. By engineering an asymmetric but periodic potential into a sample we can cause the vortex lattice to exhibit a preferred direction of motion under equal but opposite currents. Examples of asymmetric lattices can include periodic arrays of triangular pinning sites [9], which have

asymmetry due to the pinning site shape, or arrays of increasing pinning site size [63]. In these systems, an AC current will produce a DC voltage.

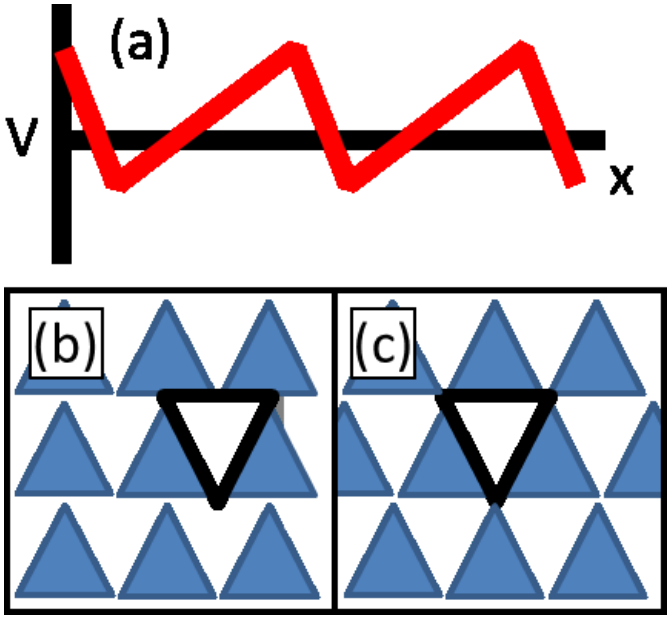

Figure 13. (a) Example of a potential that would result in rectification. Below, schematic representations of triangular pinning sites in a (b) square and (c) triangular lattice. A black line surrounds one of the interstitial areas for emphasis.

It was discovered in ref. [9] that under certain conditions the vortex rectifier can undergo a reversal of the DC voltage as a function of current amplitude. While the presence of the rectification reversal in superconducting vortex systems is now well established experimentally, its origin is controversial [64]. The following paragraphs summarize a few of those possible origins for comparison with our work:

In ref. [9] it was proposed that the reversal is due to interstitial vortices (vortices that are not on pinning sites). The authors used a sample geometry that

consisted of triangular pinning sites placed in a square lattice configuration. A reversal of the rectification was observed, but only when there were four or more vortices per pinning site. The interpretation they proposed was that three of the vortices were pinned in the triangular pinning site, while one filled an interstitial position. The interstitial areas form a square lattice of triangles in the opposite direction of the pinning sites (Figure 13b). Any rectification due to the interstitial vortices should therefore be in the opposite direction to the rectification from the pinning site asymmetry. The low driving force required to see the negative rectification further indicated that it was due to the interstitial vortices, which are not pinned as strongly as those on the pinning sites. At high driving forces the rectification reversed sign and the vortices on the pinning sites dominated the DC voltage.

A different explanation for the origin of the rectification reversal was put forth in ref. [65], where it was proposed that the vortex lattice rotates and rearranges itself into different configurations. The authors performed a molecular dynamics simulation on the vortex lattice. It was shown that for N = 4 vortices per pinning site, the vortex lattice reconfigures at high AC current amplitudes. The change in configuration occurs in order to reduce the dissipative drag by the pinning sites on the vortices (see Section I.2.2 Superconducting vortices for more details on the dissipative drag). The vortices in the new orientation can cause the DC bias to change and go through a rectification reversal at the higher AC currents. One

drawback to this explanation is the required assumption that the coefficient for the dissipative drag on the vortices is dependent on the magnitude of the external force.

In ref. [66] simulations were performed on a superconducting vortex system that claimed an order-disorder transition in the vortex lattice was responsible for the rectification reversal. Molecular dynamics simulations were performed assuming a potential that was asymmetric along the $\hat{x}$ dimension, with no dependence on the other dimension. The authors found that at low vortex densities the vortices align, forming one-dimensional chains along the $\hat{y}$ direction. They showed that this vortex configuration was the source of a positive rectification. As the vortex density was increased, the chains broke up and vortices were pushed in the reverse direction causing a negative rectification.

With these competing theories in mind, the goal of this research was to investigate the mechanism of the rectification reversal. The square lattice geometry used in ref. [9] allowed the vortices to move in one dimensional chains while remaining in either the interstitial or the pinning site areas (Figure 13b). By changing the geometry to a triangular lattice, the symmetry is broken and the interstitial vortices do not have a straight channel in which to travel (Figure 13c). For this reason we used triangular pinning sites in a triangular lattice to compare between the different competing reversal mechanisms [67].

III.2 Experiment

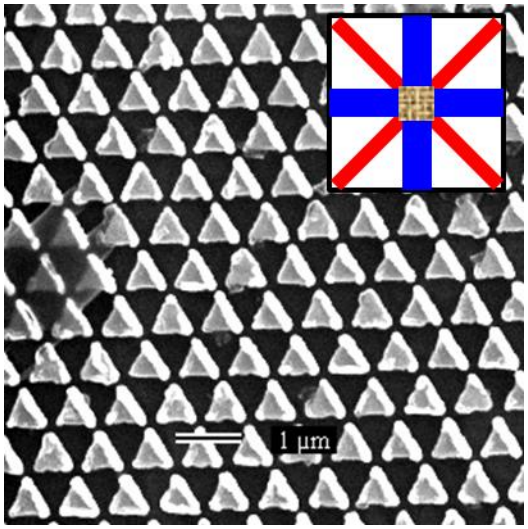

Figure 14. Scanning electron microscope picture of the triangular array of Ni triangles. The inset shows a cartoon of the sample measurement geometry. The thick vertical and horizontal lines (blue) are the current leads and the thin diagonal lines (red) are the voltage leads.

We studied several superconducting Nb films covering arrays of magnetic Ni triangles on Si (100) substrates. The equilateral triangles had sides close to 700 ± 25 nm and thickness 40 nm. They were arranged in a triangular array with a periodicity of 810 ± 30 nm. Figure 14 shows a scanning electron microscope picture of the array. Ni triangles were prepared by electron beam lithography using polymethyl methacrylate resist and liftoff. The Ni was deposited by electron-beam evaporation in a system with a base pressure of 10^{-7} Torr. A 100-nm-thick Nb film was deposited using magnetron sputtering with a base pressure of 10^{-8} Torr above the nanostructured Ni array. Electrical leads were patterned using photolithography

and etching to form a 40 μm × 40 μm bridge, which allows propagating currents and measuring voltage drops in two perpendicular directions.

The electrical resistivity of the hybrid system was measured using the standard four-point probe method, with a magnetic field applied perpendicular to the sample plane. Using this geometry, we were able to induce in-plane vortex motion parallel and perpendicular to the symmetry axes of the nanotriangles. We measured the magnetoresistance of the samples at temperatures close to the critical temperature, 8.6 K, in a liquid-helium cryostat with a superconducting solenoid and a variable temperature insert.

An alternating current ($\vec{J}_{ac}$) induces an alternating Lorentz force on each vortex, $\vec{F}_L = \vec{J}_{ac} \times \hat{z}\phi_0$ ($\phi_0$is the quantum fluxoid and $\hat{z}$ is a unit vector parallel to the applied magnetic field $\vec{B}$). Although the time-averaged force on the vortices is zero, $\langle F_L \rangle = 0$, in the presence of an asymmetric potential, a nonzero dc voltage (V_{dc}) can develop. This is the so-called rectification effect. This voltage is proportional to the time-averaged velocity, $\langle \vec{v} \rangle$, of the vortex lattice. Positive voltage (and positive vortex motion) in this work correspond to vortices moving from the base to the tip of the triangular pinning sites and the negative voltage (and negative vortex motion) appears when vortices move from the tip to the base. The rectification measurements were performed at the highest attainable frequency for our experiments (10 kHz).

III.3 Results

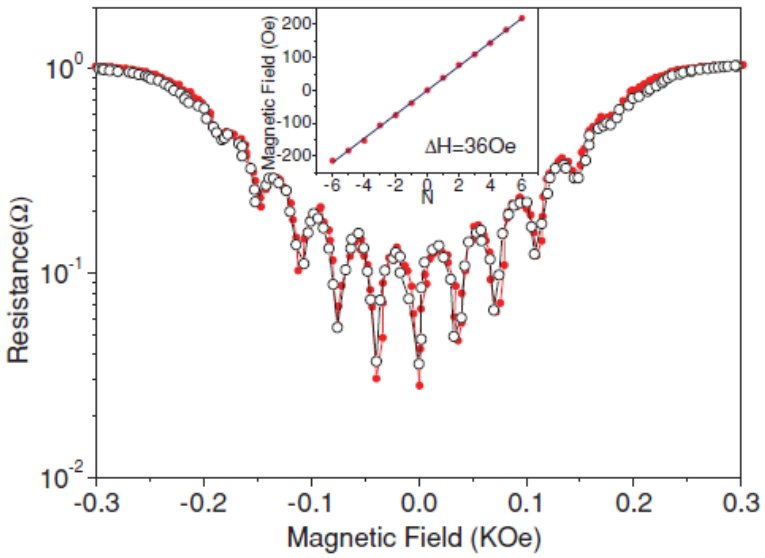

Figure 15. Magnetoresistance at T/Tc = 0.99 of a superconducting Nb thin film on a triangular array of Ni nanotriangles with the vortex driving force perpendicular (red filled circles), and parallel (black open circles) to the symmetry axes of the triangles. The superconducting critical temperature was 8.6 K. A linear fit of the matching fields shown in the inset gives ΔH = 36 Oe with a linear correlation coefficient of 0.9996. Reprinted from D. Perez de Lara et al., Phys. Rev. B 83, 174507 (2011). Copyright by the American Physical Society.

Figure 15 shows magneto-resistance measurements of the sample, an Nb film on an array of triangular pinning sites. The measurements were performed at T/T_C = 0.99 with currents both perpendicular and parallel to the symmetry axis of the triangular pinning sites. The measurements show matching minima at evenly spaced fields, ΔH = 36 Oe (inset of Figure 15). This is in agreement with the predicted value of 36 ± 3 Oe. There appears to be no difference between the matching minima positions in the parallel and the perpendicular directions.

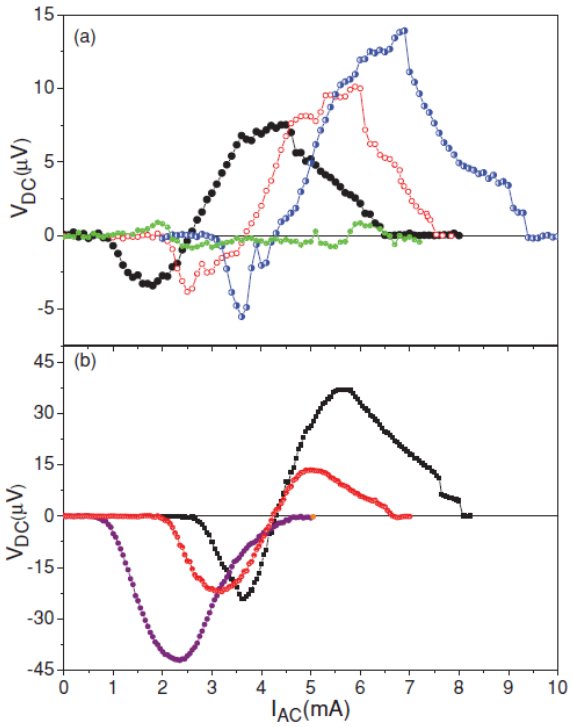

Figure 16. Rectification effect in Nb film with array of Ni triangular pinning sites and driving force perpendicular to the triangular base. (a) Several different temperatures: T/Tc = 0.99 (black filled circles), 0.98 (red open circles), and 0.97 (blue half-filled circles) and an applied field corresponding to N = 1 vortices per unit cell. For comparison, the Green circles corresponds to driving force parallel to the triangular base at T/Tc = 0.98. (b) At T/Tc = 0.97 for different magnetic fields: N = 8 (black full squares), N = 12 (red half-filled circles), and N = 20 (purple full circles). Reprinted from D. Perez de Lara et al., Phys. Rev. B 83, 174507 (2011). Copyright by the American Physical Society.

Measurements of the rectification (DC voltage) versus applied AC current amplitude are shown in Figure 16. The rectification begins at a non-zero threshold value of AC current amplitude. A negative rectification appears for all fields with $N \geq 1$, where N is the number of vortices per pinning site. The rectification reaches a minimum and then reverses sign as the current amplitude is increased. The positive rectification also reaches a maximum, and as the current amplitude is increased, goes

to zero. The reversal of the rectification can be seen for all fields up until 770 Oe (corresponding to N=20), which is close to the upper critical field 800 Oe. For comparison, Figure 16a shows the DC bias of the sample measured with the driving force parallel to the base of the triangle. In the parallel case, no rectification is visible.

As the temperature is decreased, both the positive and negative rectification effects shift to higher applied current. The maxima and minima in the rectification curves also increase in magnitude, but at higher applied currents. No frequency dependence was observed for the rectification.

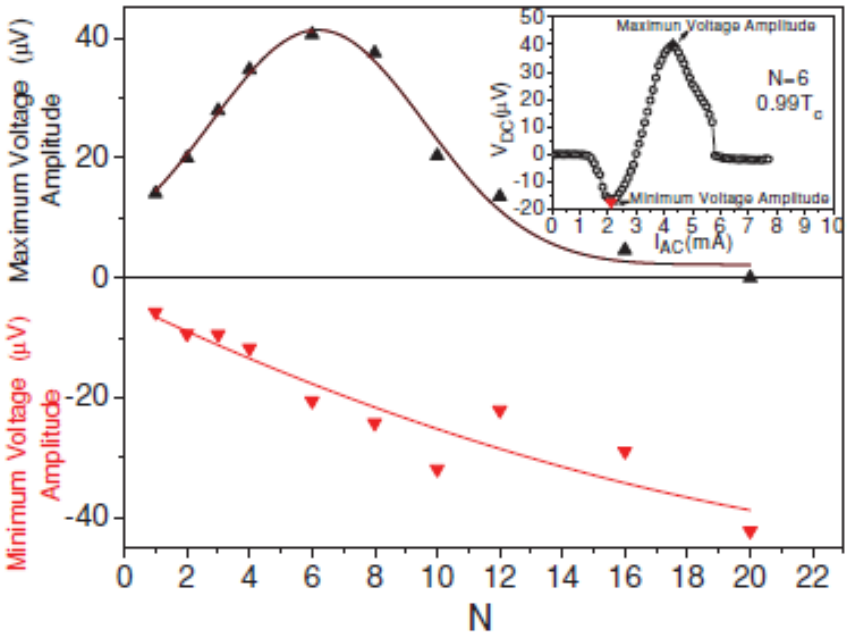

Figure 17. Maximum (black triangles) and minimum (red inverted triangles) dc voltages of the rectification effect versus N, the number of vortices per pinning site at T/Tc = 0.97. A line is added to the plots as a guide to the eye. The inset shows how the maximum and minimum voltage values are defined. Reprinted from D. Perez de Lara et al., Phys. Rev. B 83, 174507 (2011). Copyright by the American Physical Society.

Figure 16b contains several representative rectification curves taken at different magnetic fields (N = 8, 12, 20). As the field increases, there is a decrease in the onset of the negative rectification. The maxima and minima positions, and the point at which the rectification disappears, also occur at lower AC current amplitudes. However, the AC amplitude at which the rectification reverses sign appears to remain the same for the different fields.

Figure 17 shows the maximum and minimum rectified voltage values as a function of the field. The maximum voltage amplitudes have a field at which they reach a peak and then decrease in value. However, the minimum voltage amplitudes decrease approximately linearly with field.

III.4 Discussion

There is no frequency dependence to the rectification. A predicted average vortex velocity of approximately 300 m/s, given by the equation $\langle v \rangle = E/H$ [68] (where E is the average electric field, H is the applied magnetic field, and $\langle v \rangle$ is the average vortex velocity), suggests that the vortices traverse the entire sample in under a microsecond. Therefore, even at 10 KHz, the vortex flows measured are in the steady state.

Figure 16a shows no rectification effects when the vortices are traveling parallel to the base of the triangles (green circles). This indicates that the rectification is cause by the asymmetry of the triangular pinning sites. The figure also shows that as the temperature decreases, the rectifications (both negative and positive) move to

higher current amplitudes. Since pinning strengths increase with decreasing temperatures [13], higher current amplitudes are needed to reach the threshold de-pinning force.

Previously, in ref. [9] rectification was seen in a square pinning lattice geometry. However, in that geometry a rectification reversal was only seen at fields of N = 4 and above. Their interpretation for this phenomenon is that at N = 3 the vortices are interacting with the triangular pinning site and are participating only in the positive rectification. However, when another vortex is added to the unit cell it is forced into an interstitial position. The interstitial spaces form a square lattice with triangular sites that are pointing in the direction opposite the pinning sites (Figure 13b). These interstitial spaces are responsible for the negative rectification. The vortices in the interstitial spaces are not pinned as well as those on top of a pinning site. It follows that for low current amplitudes the interstitial movement dominates and there is a negative rectification. However, at higher current amplitudes, the flow of vortices in the pinning sites dominates and a positive rectification forms.

In the triangular lattice we measured a rectification reversal even at N = 1. This is surprisingly different from the square lattice case. If the negative rectification is due to the interstitial lattice, it means that interstitials are appearing at N = 1. In the square lattice this was not possible because a force on a pinned vortex would direct the vortex into another pinning site. In the case of the triangular lattice however, the force directs the vortex into an interstitial space causing the negative

rectification flow state to populate. When the forces are small, the vortices cannot re-enter the pinning sites and are therefore trapped in the interstitial lattice, contributing to the negative rectification. When the forces on the vortex lattice are high, the vortices can re-enter the pinning sites. Thus, at high current amplitudes the vortices are able to escape the negative rectification flow state and the positive rectification from the pinning site asymmetry dominates. Figure 16b shows that the rectification reversal occurs at the same current amplitude for the different fields. This implies that the force required to escape the negative rectification flow state is independent of magnetic field and is determined only by the interaction of the asymmetric pinning potential with each individual vortex.

Interestingly, if only the interstitials are contributing to the negative rectification, and assuming that at low currents they cannot re-enter the pinning sites, it would imply that the vortices move in a zig-zag motion in order to stay in the interstitial lattice. Vortices traveling in directions other than that of the driving force have previously been predicted [69] and measured [70].

Further evidence that the positive rectification is due to the vortices on the pinning sites and the negative rectification is due to the interstitials was gathered by measuring the maximum voltage amplitudes for the different rectification states at each field (Figure 17). The positive rectification shows a maximum voltage at N = 6. This value corresponds to three vortices for the triangular pinning sites and three vortices for the triangular interstitial areas. After this value, the vortex lattice

deforms too much to match to the pinning centers, and rectification is reduced. Conversely, the negative rectification has an approximately linear dependence with N, which means the voltage is proportional to number of vortices per site. If the vortices can escape the pinning centers but not re-enter them this would explain the linear dependence on the number of vortices because all of the vortices are forced into the interstitial flow states.

The interstitial lattice explanation is the most robust explanation for the origin of the rectification effects and their reversal. In the triangular lattice, chains of vortices cannot form and so an order-disorder transition cannot occur as predicted by Reichhardt et al. [63,66]. A lattice re-configuration [65] cannot explain the rectification since the lattice cannot reconfigure and still match the pinning lattice at N = 1 vortices per pinning site. The interstitial lattice explanation can account for both of these phenomena.

III.5 Summary

This chapter describes a superconducting vortex system that undergoes a rectification reversal. It was shown previously [9] that triangular pinning sites in a square lattice produce a DC rectification when an AC current is applied. Above N = 3 vortices per pinning site the rectification changed sign for different AC current amplitudes. We investigated this phenomenon further by changing the pinning lattice to a triangular configuration and found that a reversal appears even at N = 1 vortices per pinning site. We believe this means the interstitial states can be accessed at low

fields because the force on the vortices directs them into the interstitial lattice. At the low current amplitudes the vortices cannot return to the pinning sites and the negative rectification flow state is populated. Interestingly, this would mean that the vortices have to zig-zag in order to stay in the interstitial lattice.

III.6 Acknowledgments

Chapter III has been published in: D. Perez de Lara, M. Erekhinsky, E. M. Gonzalez, Y. J. Rosen, Ivan K. Schuller, and J. L. Vicent, “Vortex ratchet reversal: Role of interstitial vortices,” Phys. Rev. B 83, 174507 (2011). The dissertation author was a co-author of this paper. I would also like to thank Alicia Gomez for help with the errata for the paper. Y. J. Rosen fabricated samples for this project, corrected the length scales in the paper, wrote the errata, and worked on the explanations for the data.

CHAPTER IV

PINNING IN THE CORBINO GEOMETRY

IV.1 Introduction

Superconducting vortices are a controllable method for studying periodic systems moving in the presence of a periodic potential. The rich physics seen in these systems includes liquid and glass phases [20,71], ordered periodic lattices [21], and avalanche effects [72]. Interesting effects have also been engineered and simulated in vortex systems including flux transistors [73], rectification effects [67], and jamming [74].

The Corbino geometry [75] in particular, allows the examination of shearing forces on the vortex lattice. In this geometry, current enters a superconducting disc at the center and travels radially outwards in all directions. The current density in this geometry decreases as 1/R, where R is the distance away from the center of the disc. The radial current density produces a tangential force on the vortices, which can cause them to rotate in concentric circles. Several vortex phases have been predicted and measured in this geometry including elastic to plastic transitions [76,77], rectification due to a single flow channel [78], energy states related to vortex shell configurations [79], and irreversible flow transitions [80].

In this chapter, we explore the effects of pinning sites on vortices rotating in the Corbino geometry. When the shearing forces from this geometry are large, the

lattice is in the plastic state, where each ring can rotate at different angular velocities [76]. However, when the lattice is rotating as a rigid body, the outer regions of the lattice rotate faster than the regions closer to the center. Adding periodic pinning sites to this system can add an additional stress on the lattice due to the difference between the rotation speeds. We show that a sudden transition in the resistance occurs due to this stress when the vortex lattice is commensurate with the pinning lattice.

IV.2 Experiment

The Corbino geometry was fabricated using a five step lithography process. In the first step electron beam lithography was used to pattern a pinning array of dots on a Si substrate. The pinning sites were made of 40 nm thick Co. Each site was 250 nm in diameter with a total array radius of 30 μm. Four different pinning array geometries were used for this study. Three of the pinning arrays, a square array (Figure 18a), a triangular array, and a circular array, had a density of 6.25 sites/μm^2. The fourth pinning array, a circular array, had a density of 3.125 sites/μm^2. The circular arrays were fabricated by placing concentric rings of pinning sites every 0.4 μm (0.566 μm for the 3.125 sites/μm^2 density array). This radial separation was chosen because it is the lattice constant of a square array with the same density. The number of pinning sites in each concentric ring was chosen to keep the areal density constant throughout. The sites were placed at equal intervals along the ring with a randomly selected starting angle.

Once pinning sites were positioned on the substrate, a 100 nm thick Nb layer was deposited on top. The Nb was patterned into a Corbino disc with a diameter of 100 µm using photolithography and liftoff technique. The samples had a T_C of approximately 8 K, defined using the 90% normal resistance criterion.

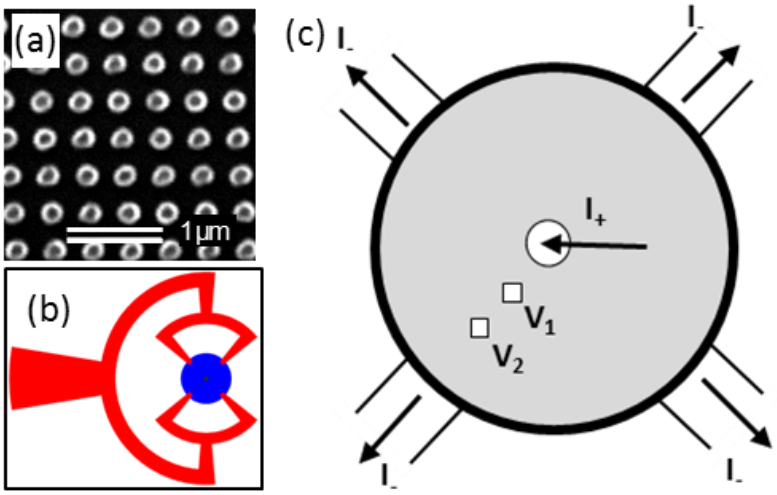

Figure 18. Geometries used for the fabrication of the Corbino system. (a) An SEM image of a square array of Co pinning sites. (b) A schematic of the outer Au contacts (red) connected to the Nb Corbino disc (blue). (c) A schematic of the corbino disc. The current enters through the center (I_+) and leaves from the edges (I_-). The voltage taps are placed at positions V_1 and V_2 at radii 17.5 µm and 31.5 µm respectively. Top Au contacts are connected to I_+, V_1, and V_2 from the top. There is a SiO_2 insulating layer in between the Nb disc and the Au contacts.

Au contacts with a thickness of 90 nm were placed on the Corbino disc with a 10 nm Ti adhesion layer on top (the red area in Figure 18b). The Au contacts were patterned so that current paths leaving the disc were equidistant. Small Au contacts on the edge of the Corbino disc were used so that the current profile could be determined exactly using a partial different equation (PDE) solver (Figure 19), and

non-radially symmetric areas could be identified. Another option would have been to use large rings of conducting material on the disc edges [81]. While this geometry is ideal for measuring a thin channel, it requires the assumption that the electric potential is uniform over the large ring. This is not true when the contact resistance is very small, for example in the case where the proximity effect causes the Au contacts to become superconducting.

The fourth lithography step consisted of depositing a SiO_2 disc, 340 μm in diameter and 80nm in thickness centered on the Corbino disc. Three holes were patterned into the SiO_2 (Figure 18c): one current tap (denoted by I_+) at the center of the disc with radius 5 μm, and two square voltage taps with edge length 3 μm placed at distances 17.5 μm (V_1), and 31.5 μm (V_2) from the center. In this geometry, current can enter through the center contact, I_+, travel radially outward and exit through the outer contacts, I_- (Figure 18c). Contacts V_1 and V_2 are used for voltage measurements. A final layer of lithography is used to place 100 nm of Au to contact the holes in the SiO_2 and the I_- layer. Care is taken to reduce the amount of insulating SiO_2 area needed to reduce the probability of pinholes.

The current distribution was modeled with the Matlab PDE solver in Figure 19. A Corbino disc with constant conductivity and the sample contact positions was inputted into Matlab. Distances in the model are scaled 1:100 μm. The position of the voltage tap, V_2, at 31.5 μm corresponds to the boundary between the radially

symmetric and non-radially symmetric voltage distributions. The inner voltage tap, V_1, at 17.5 µm is within the radial current distribution area.

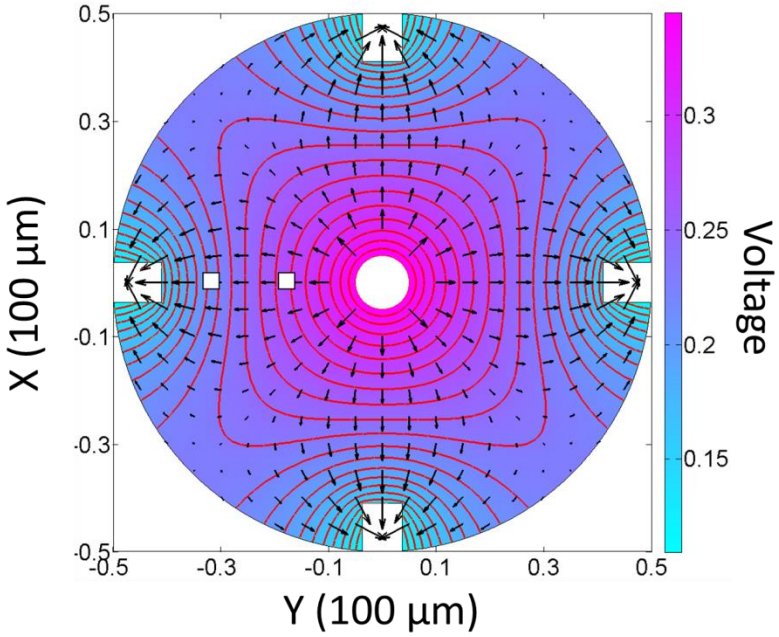

Figure 19. Current and voltage distribution simulated for a Corbino disc with a circular geometry and homogeneous conductivity. 1 on the x-axis and y-axis scale bars corresponds to 100 µm on the Nb Corbino disc. The color bar corresponds to different electrical potentials with equipotential lines (red) drawn on the disc for clarity. Arrows (black) correspond to the magnitude and direction of the current. Two white squares have been added at the voltage tap positions.

Magnetoresistance measurements were conducted in a variable temperature liquid-He flow cryostat with temperature stability better than 1 mK. The resistance was measured using a current source and nanovoltmeter in standard dc polarity reversal mode [38]. In this mode, the current oscillates in a square wave pattern and automatically triggers the voltmeter in order to reduce the noise and voltage drift. Assuming a steady state, the positive and negative currents should only cause a

reversal of the vortex rotation direction. The magnetic field was controlled using a Cryomagnetics Inc. 4G superconducting magnet power supply with a precision of ±1 Gauss.

IV.3 Results

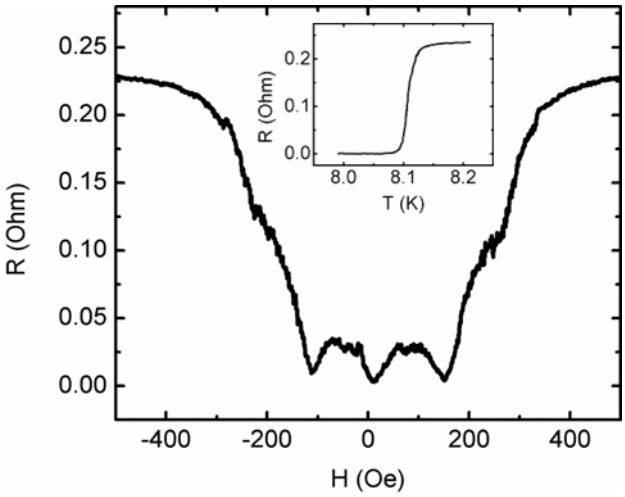

Figure 20. Magnetoresistance measurement in the 4-point configuration over a square array of pinning sites. Voltage was measured between leads V_1 and V_2 at T/T_C=0.995. The inset shows the resistance versus temperature for the same measurement configuration.

Measurements in the 4-point current/voltage configuration were performed on the Corbino disc for a variety of temperatures. The resistance versus temperature curve shows a three order of magnitude transition over 50 mK (inset of Figure 20) with T_C = 8.1 K. At T/T_C = 0.995 the magneto-resistance measurements show the presence of matching minima consistent in position with those seen when current is passed uniformly over the sample (Figure 20). Second and third order minima appear

for higher temperatures where the sharp transition is moved to higher fields (not shown).

Figure 21 shows magneto-resistance measurements for the Corbino geometry measured in the 3-point configuration. The current is passed between the I_+ and I_- contacts and voltage is measured between the V_1 and I_+ contacts. In this configuration the lead resistance is included in the measurement but it allows access to the physics occurring at smaller radii. The inset of Figure 21 shows the resistance versus temperature at zero field. The resistance has a quick drop at T_C but unlike the 4-point configuration, the resistance continues to decrease slightly even at low temperatures. This could be due to the proximity effect causing the Au contacts to become superconducting.

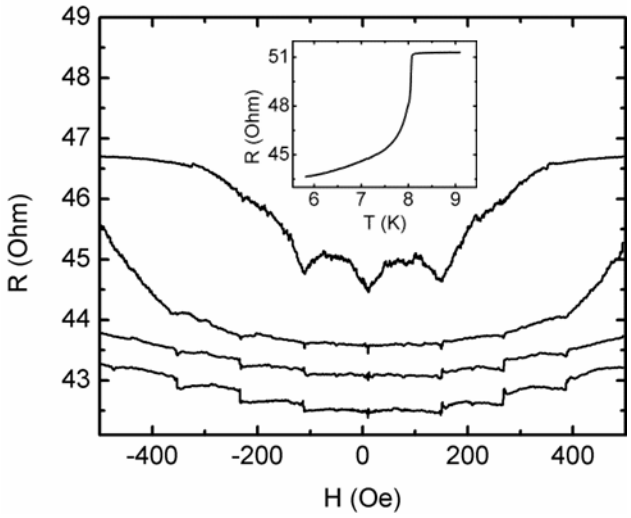

Figure 21. Magnetoresistance measurements in the 3-point configuration over a square array of pinning sites. Voltage was measured between the I_+ lead and the V_1 lead. T/T_C for the different curves from top to bottom are: 0.998, 0.992, 0.987, and 0.980. The inset shows the resistance versus temperature for the same contact configuration.

The T_C is defined as the temperature at which the transition has decreased the resistance to 90% of the normal resistance. The T_Cs of the 3-point configuration were calculated by treating the minimum measured resistance as the lead resistance. This number is not entirely accurate since we were not able to go to the minimum value of the transition, however the error is considered small because close to T_C the resistance changes by 1 ohm/20 mK.

The magneto-resistance curves shown in Figure 21 were measured at T/T_C = 0.998, 0.992, 0.987, and 0.980. The top curve, measured at the highest temperature, shows minima corresponding to the 4-point configuration. As the temperature is decreased, the amplitude of the minima becomes small and the minima become narrower. As the temperature continues to decrease, the minima evolve into steps at the matching fields, with plateaus in between those fields.

The steps in the resistance were explored as a function of magnetic field in Figure 22. The graph in (a) shows the resistance measured as a function of time while the field, shown in graph (b), was varied. The field was changed in small increments around the second matching field to determine the properties of the step. When the field was below 264 Oe (shown in blue) the resistance was consistently at the bottom of the step (below the black line in Figure 22a). When the field was above 265 Oe (shown in green) the resistance was consistently at the top of the step (above the black line in Figure 22a). At the transition, the resistance showed a median value that was either at the top of the step or at the bottom of the step, but never in between.

It is interesting to note that when the magnetic field was stabilized close to the transition, the resistance occasionally showed an increase in noise in the direction of the step. There was no hysteresis measured in the transition to within 1 Oe.

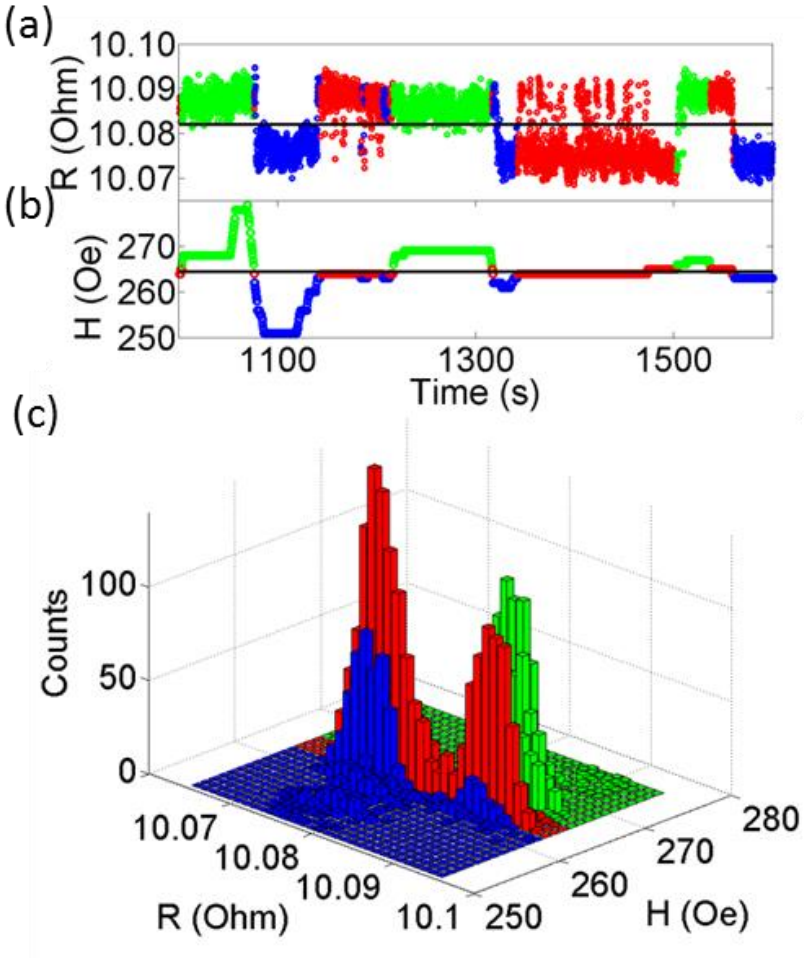

Figure 22. (a) Resistance as a function of time for different fields. The black line is a guide to the eye between the high resistance and low resistance modes. (b) The field on the sample at the different times. The black line at H=264.5 Oe is a guide to the eye to denote the approximate transition field. (c) Histogram of the number of counts for each resistance and field. In the above graphs, for fields above 265 Oe the points are shown in green, below 264 Oe the points are shown in blue, and for fields between 264 and 265 points are shown in red.

Figure 22c shows a histogram of the number of counts for each resistance and field. The coloring scheme is the same as in parts (a) and (b). When the field is low (high), the resistance is low (high) as well. When the field is at the transition, the resistance shows a bi-modal distribution. No resistance state can be seen in between the top and bottom resistances of the step.

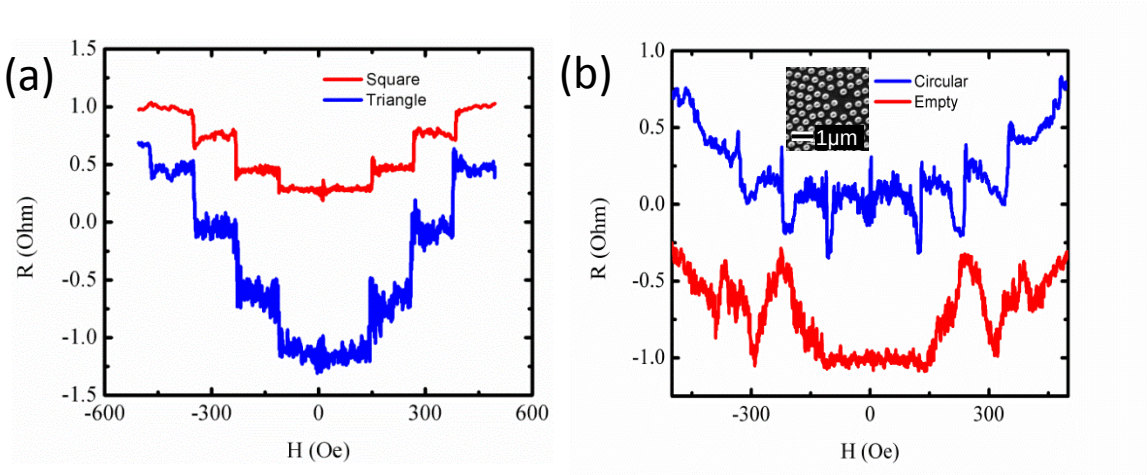

Figure 23. Magnetoresistance of different lattice types in the step regime with a 3-point configuration. (a) A square pinning array (shown in red) at $T/T_C = 0.955$ and a triangular pinning array (shown in blue) at $T/T_C = 0.933$. (b) A circular pinning array (shown in blue) at $T/T_C = 0.995$ and a blank sample with no pinning centers (shown in red) at $T/T_C = 0.872$. The inset shows an SEM image of the circular pinning array. All curves have had their lead resistance subtracted and have been shifted along the y-axis for clarity.

Figure 23 shows the low temperature magneto-resistance curves for a square, triangular, and circular pinning lattice in addition to an empty sample with no pinning sites. The lead resistance has been subtracted and the curves have been shifted about the y-axis for clarity. The temperatures of the curves have been chosen so the samples are in the step regime. The square and triangular arrays show well-defined

steps at the matching fields with plateaus in between. The circular array shows a minimum when the matching field is approached from the low field side, however the sharp increase is still present at the matching fields and raises the resistance to some background value. No plateau is present in the circular pinning site case. The empty sample does not show steps. Instead, there is a plateau around zero field followed by repeatable oscillations well above the noise level. These oscillations change in position slightly with temperature.

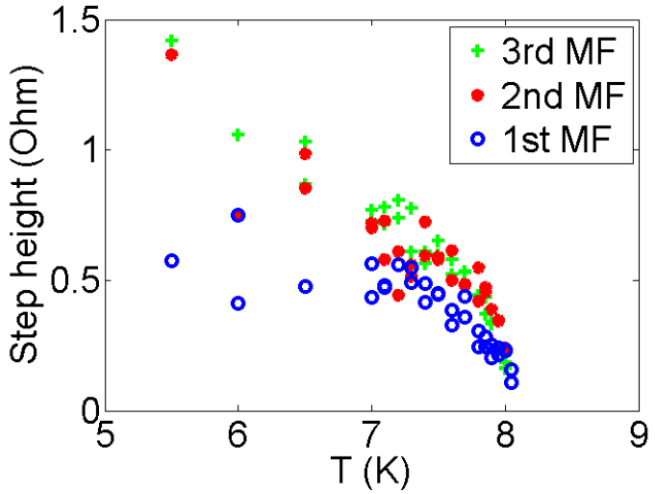

Figure 24. The height of the steps as a function of temperature for a triangular pinning lattice with T_C = 8.1 K. The different shapes and colors correspond to different matching fields (MF) as indicated by the legend.

Figure 24 shows the height of the step as a function of temperature for different matching fields. As the temperature is reduced the step height increases, although noise in the measurements also increases. Additionally, a general trend is observed for the different samples where the step at the first matching field is smaller than the steps at the second and third matching fields.

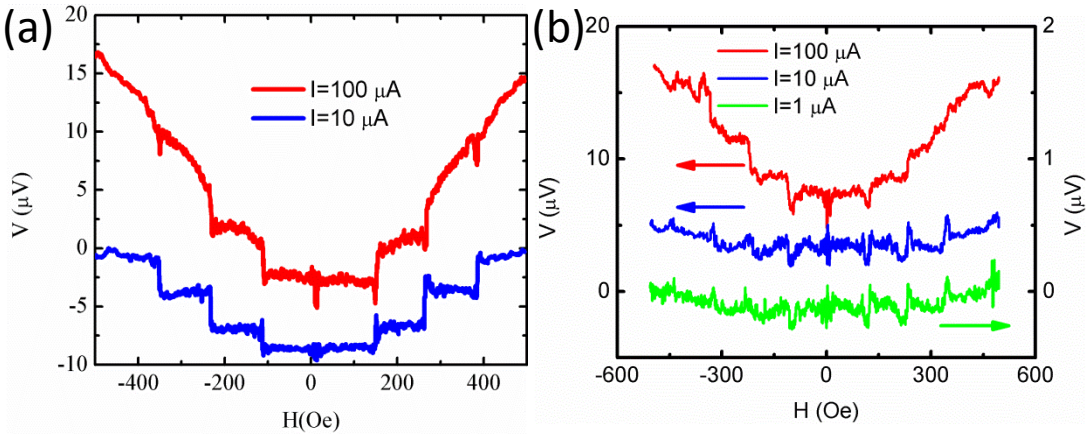

Figure 25. Voltage as a function of magnetic field for different currents. The curves have been shifted along the y-axis for clarity and to remove the lead resistance. (a) Square pinning site lattice. (b) Circular pinning lattice. The bottom curve corresponds to the axis on the right while the top two curves correspond to the axis on the left.

Figure 25 shows the voltage versus magnetic field at several different currents. Figure 25a shows the dependence for a square lattice. The step heights are within a factor of two in the voltage scale, even though the current was changed by a factor of 10. Figure 25b shows the several currents for a circular lattice. For I = 100 μA and I = 10 μA (corresponding to the left axis) the step height is approximately the same in the voltage scale. When the current was I = 1 μA (right axis) the step height was approximately 10 times less in the voltage scale, or in other words, approximately the same resistance as the I = 10 μA curve. Current versus voltage measurements were attempted below and above the steps however there was too much noise and drift in the voltmeter.

IV.4 Discussion

Two theories are presented to explain the results. First, a shearing transition of the vortex lattice will be discussed. In ref. [76] the presence of two regimes is extracted from the data, the elastic regime at low temperatures and the plastic regime at high temperatures. In the elastic regime, the vortex-vortex interaction dominates and the lattice is rigid. Although the lattice can rotate, it does so collectively with the same angular velocity. In this state, the outer radii have greater speeds than the inner radii. In the plastic state, the gradient of the current forces the vortex lattice to shear tangentially. Rotating rings of vortices move independently with different angular velocities.

At high temperatures when the system is plastic, each vortex ring can be treated as a separate system. If the density of the rotating ring matches the density of the pinning lattice occupying the same area, the vortices will pin and there will be minima in the magneto-resistance curves. This is why at high temperatures Figure 20 and Figure 21 show minima at the matching fields.

At low temperatures, ref. [76] claims the vortex lattice becomes elastic. In the elastic regime the outer vortices move at higher speeds than the inner vortices. Consequently, the outer vortices will encounter more pinning sites per unit time than the inner ones. The increase in pinning creates a shearing force on the vortex lattice. For sufficiently strong pinning sites this leads to a shearing of the lattice causing the inner area to increase its angular velocity, ω, according to the equation [77]:

$$\omega \propto \frac{1}{R^3} \quad \text{(IV.1)}$$

where R is the radius of the elastic disc of vortices. Even if the outer sheared shell of vortices is completely pinned and contributes no voltage, the increase in angular velocity of the inner shell gives

$$\boldsymbol{Voltage} \propto \frac{\mathbf{1}}{\boldsymbol{R}}. \quad \text{(IV.2)}$$

When a shearing transition occurs, the radius of the elastic regime vortices decreases, and the measured voltage increases. The steps seen in the magneto-resistance curves could be caused by such a transition. This scenario also explains the lack of steps in the Corbino geometry with no pinning array for the vortices to drag upon.

The temperature dependence can be explained as follows. As the temperature is decreased, the vortex lattice becomes more rigid and is difficult to shear. However when the lattice does shear due to the matching condition, it produces a higher voltage step because it is forced into the sheared state and can move much more freely. Similarly, when the field is increased more vortices contribute to the rotation and so the steps are bigger.

Another possible scenario is that there is a ground state consisting of vortex shells where each shell contains a 'magic number' of vortices according to its radius. This scenario was found in simulations performed in ref. [82]. In this simulation, the authors saw hysteresis as a function of current when transitioning between the

different shells. While we could not perform I-V measurements, the lack of hysteresis as a function of magnetic field tends to rule out this scenario.

The shearing transition theory is favored by this dissertation because it explains the steps and is supported by previous experimental studies in the subject. In order for future experiments to test the validity of this theory, more voltage contacts must be placed on the superconducting disc. If the voltage from different points can be measured, a shearing transition where the angular velocity abruptly changes at the matching fields should be seen, similar to the geometry in [76].

Regardless of the origin, these steps can be used as a superconducting switching device. The switching fields can be tailored using quasi periodic pinning structures so that many magnetic fields can be used [31]. The discretization of the resistance and the sharpness of the transition are advantageous for applications such as negative feedback devices and logic gates.

IV.5 Conclusions

Vortex dynamics were measured in the Corbino geometry under the influence of a pinning lattice. At high temperatures, matching minima from the pinning lattice were seen at the predicted magnetic fields. At low temperatures, the matching fields show steps rather than minima. The steps are bi-modal with no state in between the two levels. We believe these steps are due to a shearing transition in the elastic vortex lattice. The transition causes an increase in the angular velocity of the inner sheared area, which in turn causes a step in the voltage.

IV.6 Acknowledgements

Chapter IV is currently being prepared for publication. Co-authors include S. Guenon and Ivan K. Schuller. The dissertation author was the primary investigator and author of this material. Y. J. Rosen worked on the sample design, performed the fabrication, measurement, analysis, and simulation for this work, and will be the primary author on the paper.

CHAPTER V

ONGOING VORTEX PINNING PROJECTS AND COLLABORATIONS

V.1 Pinning boundary effects

V.1.1 Introduction

Vortices entering a pinning site lattice can cause a host of interesting vortex dynamics such as collective pinning [23], fractional matching effects [83], quasi-periodic pinning [31], and even bi-stability [8]. Vortices that enter pinning lattices are also predicted to have jamming [69] and channeling [84] effects in the vortex flow. The conditions for most of these different effects are dependent on the pinning site configuration and density. Adding an artificial boundary separating two different pinning lattices can cause these effects to be enhanced and the vortex lattices to interact between the different pinning regimes. The goal of this project was to investigate boundary effects due to two different pinning lattice types in close proximity.

V.1.2 Experiment

The pinning lattices were patterned using e-beam lithography and the liftoff technique to make Co circular pinning sites with a height of 40nm. 100nm of Nb was then deposited by MBE. Photolithography and reactive ion etching were used to pattern the Nb into contacts arranged in a 4-point measurement configuration.

The measurements were performed in a Janis cryostat with temperature stability of 10 mK. They were carried out using the standard 4-point measurement configuration with current densities ranging from 0.02-200 kA/cm^2. To take a data point, the magnetic field was stepped in 5 Oe increments, stabilized, a constant current was applied to the sample, and the voltage was measured.

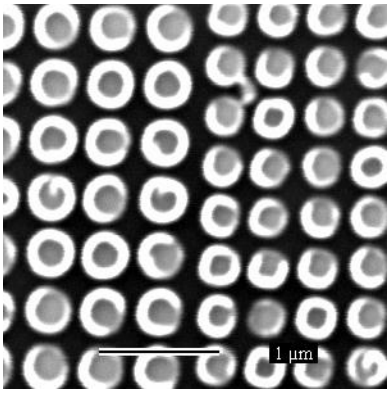

Figure 26. Scanning electron microscope image of sample 34 showing the boundary between two different pinning site lattices with spacing 445 nm and 510 nm. In this system the size of the pinning sites was changed between the different lattice spacings to preserve the filling fraction of the pinning material.

Several different lattice configurations were chosen. The pinning lattices were placed in a 67 x 67 µm^2 area with the lattice changes happening in stripes along one dimension. While the total pinning area was kept constant, the periodicity of the stripes was changed for different samples (Table 2). Among the different alternating striped geometries chosen were samples with lattice spacings that had a factor of two difference between them, lattice spacings with an irrational number (*e*) factor between them, rotated lattices, and triangular-square lattice types in the same

sample. Figure 26 shows an SEM image of one such configuration where the square lattice parameter alternated between 445 nm and 510 nm.

Table 2. Samples measured for pinning boundary project. Two or more samples were made for each geometry to add redundancy to the fabrication process. Different lattice spacing and types were varied along one dimension. The different lattice types consisted of Square (S), Hexagonal (H), and square at a 45° angle (D). The slash denotes the parameters varying in the sample.

Sample #	Lattice type	Spacing (nm)	Period (μm)	Sample #	Lattice type	Spacing (nm)	Period (μm)
5,6	S	335/670	18	23,24	H/S	560	18
7,8	S	445/890	18	25,26	S	560	18
9,10	S/H	445/480	18	27,28	H	560	18
11,12	S	335/910	18	29,30	S	445/510	18
13,14	S/H	445	18	31,32	S	445 Large Dots	18
15,16, 21,22	H	445	18	33,34	S	445/510 Large Dots	18
17,18	D	445	18	35,36	S	445/510	0.9/18
19,20	S	445	18	37,38, 39,40	S	445/510	2.2/18

V.1.3 Results

When measured, the matching effects from each density added linearly to the other matching effects. One typical example is sample 34 where the lattice parameter of the pinning sites alternated between 445 nm and 510 nm corresponding to matching fields of 104 ± 5 Oe and 80 ± 4 Oe respectively (errors are due to uncertainty in scale of SEM image). Magneto-resistance measurements of the sample were taken for several different temperatures and current densities (Figure 27). Minima appeared in the magneto-resistance data with matching fields every 110 ± 1 Oe and 85 ± 1 Oe. These minima are in good agreement with the predicted

values. There was also hysteresis in the magneto-resistance curves when the field was swept in opposite directions. However, any contributions from the pinning sites were too small to be differentiated from the hysteresis in the superconducting magnet.

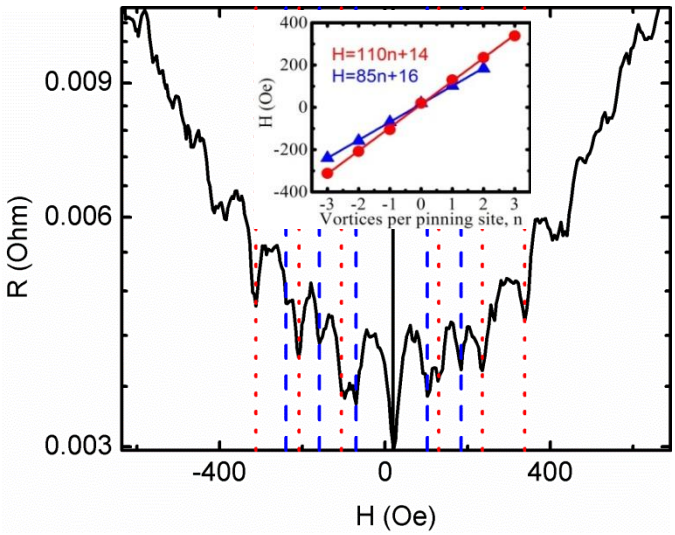

Figure 27. Magneto-resistance curve for sample 34 with alternating square lattice spacing of 445 nm and 510 nm. Dotted (red) and dashed (blue) lines denote the positions of the matching fields. The inset shows the matching field positions extracted from the curve as a function of vortices per pinning site for each density. A line is fit to those values and the matching field values of 110 Oe and 85 Oe are extracted.

One interesting effect seen was in sample 8, which has very large density changes. Figure 28 show the I-V characteristics for high current densities (above 200 kA/cm^2) in sample 8 with lattice spacing alternating between 445 nm and 890 nm. The graph shows several magnetic fields ranging from 0 Oe (Figure 28a) to 1000 Oe (Figure 28d). The zero field graph shows only one superconducting

transition, however at higher magnetic fields multiple transitions appear in the I-V curves.

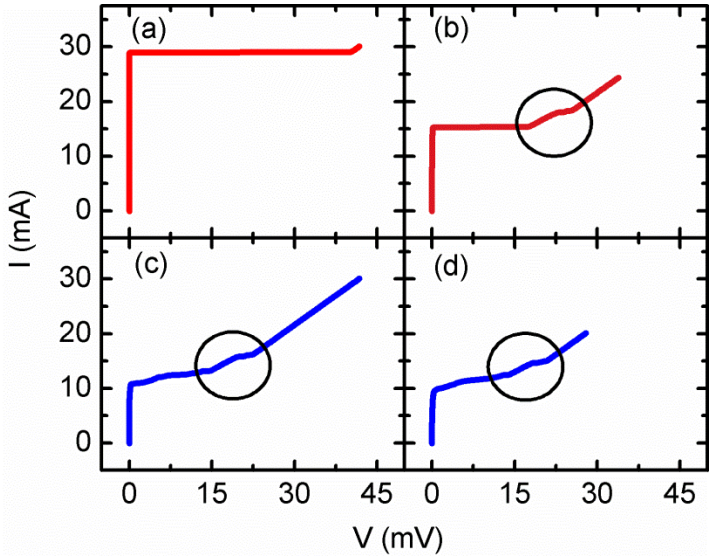

Figure 28. Voltage versus current of sample 8 with pinning site lattice spacing alternating between 445 nm and 930 nm. The current was ramped from 0 to 30 mA and measured using a voltmeter. The different graphs correspond to different magnetic fields: (a) 0 Oe, (b) 200 Oe, (c) 700 Oe, (d) 1000 Oe.

V.1.4 Discussion

Pinning occurs when the vortex lattice density matches some fraction of the pinning lattice density, leading to a dip in the resistance. Figure 27 shows one such case where pinning occurs every 85 Oe independently of the pinning that occurs every 110 Oe. Any boundary effects from the vortex lattice moving into another pinning landscape are either too small to see above the noise or else non-existent. This suggests that the pinning interaction in the ordered pinning lattice is not strong enough to disorder the vortex lattice.

Another conclusion from this project is that the pinning sites do affect the critical current of the local superconducting material. The different jumps in Figure 28 are probably due to weak links in the superconductor which have a reduced critical current. This effect is strongest when the pinning site densities are very different as seen in Figure 28 where the pinning site densities differed by a factor of four.

Although the results of this project are not novel, a future project is planned to measure conformal mapping configurations on pinning sites. In this system the density of the pinning sites is changed continuously as a function of position. Computer simulations on this system suggest the current density may be enhanced for the continuous region of magnetic fields [85].

V.2 Magnetic susceptibility measurements

V.2.1 Introduction

Surface boundary effects play an important role in most condensed matter systems. In superconductivity they are responsible for phenomena such as Little-Parks oscillations [86], Josephson junctions [87], and superconducting diamagnetism [1]. In superconducting vortex systems the Bean-Livingston barrier [88] prevents vortices from exiting the superconductor and causes hysteresis in magnetization curves. Additionally, this creates a system where a threshold value of field must be applied before a vortex can enter the superconductor and so under certain conditions avalanches of vortices jump into the superconductor [89].

Boundary effects play an important role in superconducting vortex dynamics. When the magnetic field is increased, the vortices entering the superconductor must do so from the boundaries. If other vortices are present in the system, they compress to allow the vortices at the boundaries to enter. If there are pinning sites there will be an additional barrier impeding the entrance or exit of new vortices. The barrier, and therefore the pinning, can be studied through AC magnetic susceptibility measurements [51,90].

AC Magnetic susceptibility measurements allow vortex pinning to be studied at very low temperatures. At these temperatures the resistance of the sample is effectively zero so this method allows us to investigate properties of the vortex lattice that transport measurements cannot detect. One such example is reported in [51] where hysteretic pinning effects are measured due to the competition between intrinsic pinning sites and artificial pinning sites. Intrinsic pinning sites are strong at low temperatures when there is little resistance so the AC magnetic susceptibility measurements are an ideal method for studying them.

AC magnetic susceptibility measurements are performed using a vibrating sample magnetometer. Both an AC and a DC magnetic field are applied to the sample. The DC field is typically large, and has a range of 1 Tesla which allows us to measure at the matching fields. The AC field, typically on the order of 1 Oe, oscillates at a frequency of 1 KHz. This alternating magnetic field adds and removes one vortex per 5 X 5 μm^2 every period. The magnetic susceptibility, which is measured with a

lock-in connected to the AC field, gives a measure of the number of vortices able to deform the vortex lattice and enter the superconductor.

V.2.2 Disordered arrays of pinning sites

This research project is intended to expand on work done in ref. [51]. The vortex lattice in the report interacts with both intrinsic pinning sites and artificial pinning sites. The intrinsic pinning sites are due to grain boundaries, defects, and even the changes in the volume and elastic constants when a material becomes superconducting [91]. These pinning sites increase in strength at low temperatures where they can pin the vortex lattice and trap the flux inside, which is the source of the well-known quantum levitation effect [92]. In order to study the intrinsic pinning sites, the authors in ref. [51] placed artificial pinning sites underneath a type II superconductor and studied the interaction of the vortex lattice with the different types of pinning present in the sample. To expand on this research, we increased the amount of disorder in the artificial pinning lattice to make it resemble that of the intrinsic, randomly located, pinning sites.

Three samples were fabricated. Two of the samples were made with a range of local order (For an explanation of the RLO and PCF see section II.2.2 The two dimensional “parking” algorithm) greater than 500 nm using the porous alumina technique with the standard two anodization process (see section I.3.2 Porous alumina masks for a description of the process) [34]. The third sample was fabricated using only one anodization to decrease the order of the pinning sites. The pair

correlation function for the three samples is shown in Figure 29. The figure shows a large decrease in RLO for the single anodization sample.

The samples fabricated are currently awaiting measurement.

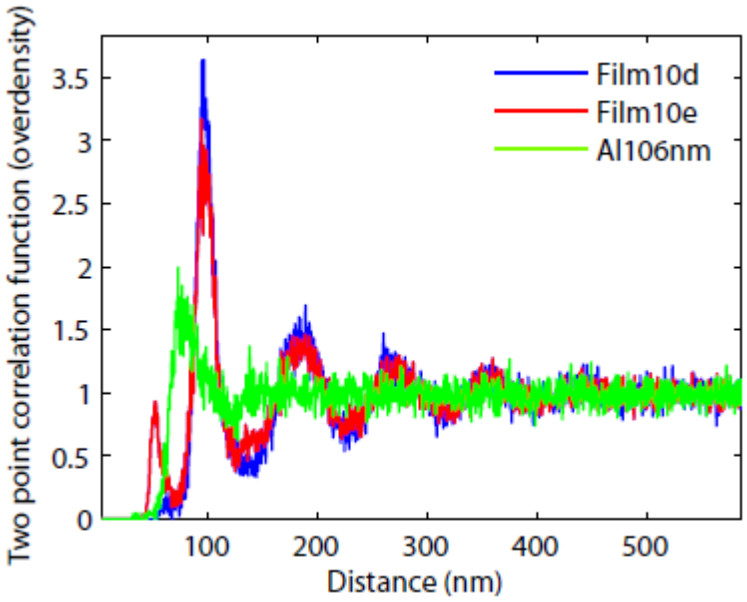

Figure 29. Pair correlation function for three different samples. Film 10d and 10e were made with the maximum possible order generated with secondary anodization. Sample Al106nm was generated with one anodization.

V.2.3 Arrays of superconducting pinning sites

One way to study the vortex lattice is to engineer repulsive sites into the superconductor rather than attractive pinning sites. If a site is repulsive it could block vortex flow, force the vortices to move along channels, or distort the vortex lattice. Creating repulsive regions can be achieved by placing superconducting sites in contact with the superconducting thin film. The field lines from a vortex on a

superconducting site will have to bend around the superconductor, which is energetically unfavorable. This suggests that the vortices should repel from those areas.

Two experiments were performed using superconducting sites. In the first, Nb dots were fabricated using e-beam lithography. The circular sites were approximately 250 nm in diameter and 40 nm in thickness. Nb was deposited on top of these sites and patterned into a resistance bridge. Two different geometries were tested: a honeycomb lattice and a square lattice.

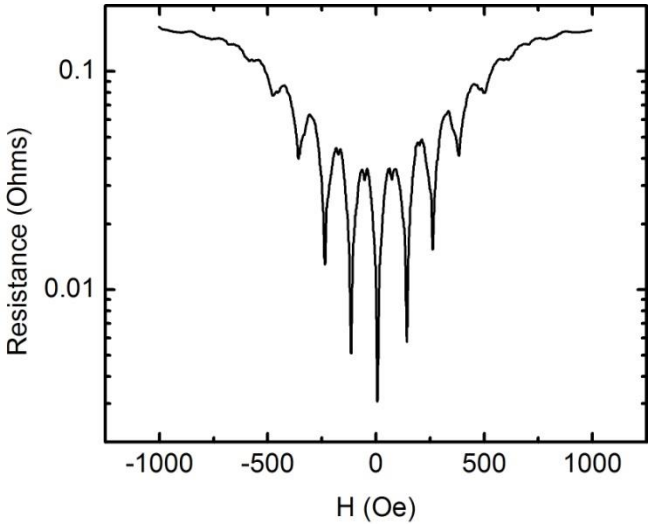

Figure 30. Magneto-resistance curve for a Nb film covering Nb dots. The matching effects in the curve match the density of the pinning sites.

Figure 30 shows a typical magneto-resistance curve for the superconducting pinning sites. The curve show standard matching effects, identical to those seen when Co pinning sites are used. The corrugation in the film appears to be a source of strong pinning which overcomes any repulsive effects. It is possible that the Nb

columns were decoupled from the Nb film due to an oxide layer or surface defects, and their Tc was depressed due to their size. If the dots were not in the superconducting state when the measurements of the film were taken it would explain why no repulsion was measured.

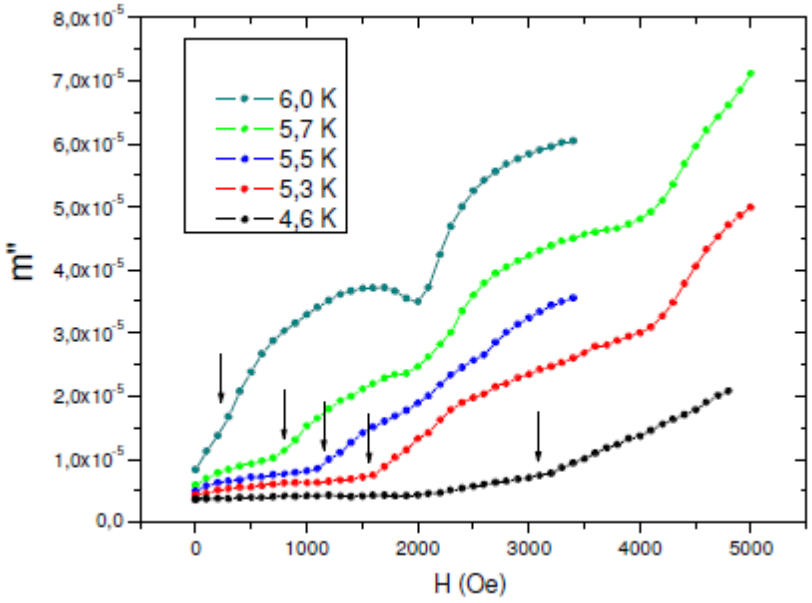

Figure 31. AC magnetic susceptibility measurements of a lattice of Vanadium dots covered by a Nb film. The graph shows the out of phase component of the AC magnetic susceptibility as a function of DC magnetic field. The different curves are taken at different temperatures. Arrows have been added to the graph to highlight a kink which appears to change position as a function of temperature.

In order to ensure the sites were in the superconducting state, the measurement must take place at low temperatures. For this reason we measured samples using the AC magnetic susceptibility method. To measure this effect, samples of Vanadium sites (Vanadium was used due to difficulty lifting off the Nb with porous alumina) were made using the porous alumina technique and then

covered with a Nb film. Measurements of the AC magnetic susceptibility were then performed as a function of magnetic field for several different temperatures.

Figure 31 shows the out of phase component of the AC magnetic susceptibility measurements as a function of the DC magnetic field for several different temperatures. The first and second matching minima are present at higher temperatures appearing at the predicted 2000 Oe and 4000 Oe respectively. Additionally, another transition occurs where the slope of the curve changes abruptly. The transition point has been marked by an arrow for the different temperatures. The real part of the AC magnetic susceptibility showed the same features but they were less pronounced.

There are currently two competing interpretations for the origin of the transition. In the first interpretation, the transition occurs when the Vanadium dots become superconducting at H_C. As the temperature is decreased, H_C is expected to move to higher fields [1]. It is important to note that H_C does not have to be the same value as a pure Vanadium film. This is due to the proximity effect, which is suppressing the Tc of Nb, and transitioning the Vanadium into a superconducting state at higher temperatures. The superconducting Vanadium sites lock the vortices into position, preventing them from moving out of their interstitial areas. This increase of pinning prevents the entrance of new vortices into the Nb film, and reduces the AC magnetic susceptibility of the sample.

The second interpretation is that some effect (for example corrugation or the proximity effect) is causing different transition temperatures to appear for different areas of the superconductor. At low temperatures, even though the bulk of the Nb is in the superconducting state, some areas may not have transitioned yet. These areas could be the cause of the non-zero AC magnetic susceptibility, and the low temperature transition point could be the areas becoming superconducting.

Measurements are continuing on new samples to determine the correct interpretation of these initial results.

V.3 Neutron scattering

Neutron scattering is another method able to measure vortex dynamics below the resistive transition. Neutrons are sensitive to the magnetic field deviations in the superconducting vortex. By scattering neutrons off the magnetic inhomogeneities in a Nb sample, information about the vortex lattice can be gathered. For example, an experiment was performed in ref. [93] where a bulk single crystal of Nb was measured while vortices were present in the sample. A Bragg peak was seen and both horizontal and vertical disorder could be measured in the sample.

In our experiment we want to study the interaction of thin film, two-dimensional vortices with pinning sites. To accomplish this, a large array of pinning sites was created using the porous alumina technique (see section I.3.2). The pinning sites were made out of Cu due to its large neutron scattering length. The sample was

then covered with Nb. Several equally sized samples were fabricated with this process so that they could be stacked and increase the signal quality.

The experiment will be performed as follows: neutrons will travel perpendicular to the plane of vortices and pass through several silicon pieces. When above Tc they will interact with the ordered Cu lattice and should produce a Bragg peak due to the periodicity in the Cu sites. If below Tc, we expect a secondary peak due to the ordered vortex lattice. As the density of the vortex lattice approaches the density of the Cu sites there should be some interaction between them.

In another experiment we will apply current to the sample while in the superconducting state. Since the vortices are flowing, each neutron will pass through the sample and see a different vortex configuration. However, if the vortices are pinned the vortex lattice should be the same for the different neutrons. The neutron scattering signal should therefore give us insights into the pinning strength and vortex flow patterns.

Samples for this experiment have been fabricated and are currently awaiting measurement.

V.4 Magnetic force microscopy of the vortex lattice

One drawback to the other methods presented in this chapter is that the position of the vortices cannot be ascertained. The pinning potentials between the vortices and the pinning sites can be estimated [27] but still remain largely unknown. It is even unclear whether the vortices prefer to sit on the pinning sites or in the

interstitial positions. This lack of information limits our understanding of the phenomenon and only general conclusions about the way a vortex interacts with a unit cell of the pinning lattice can be made. To address these concerns we are imaging the vortex lattice with a Magnetic Force Microscope (MFM).

In atomic force microscopy a cantilever with a small tip scans across the surface of a sample and measures height variations through the vibrations of the tip. An MFM operates in much the same way except the tip is coated with magnetic material and is sensitive to stray magnetic fields. In the case of a vortex lattice the MFM is able to distinguish between areas of flux penetration (superconducting vortices) and the superconducting regions [94].

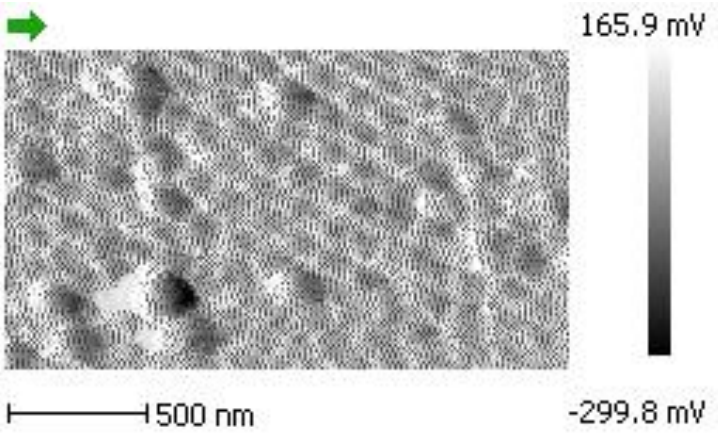

Figure 32. MFM image of Nb thin film on top of Co pinning sites. The sample was cooled to 4 K and a magnetic field of 2000 Oe was applied.

Samples of Co pinning sites were fabricated using the porous alumina technique (see section I.3.2). A large area of pinning sites, greater than 1 X 1 mm^2 is required because there is no optical microscope for alignment of the MFM tip. After

the sample is fabricated it is inserted into a low temperature MFM and the tip is scanned at several different fields and temperatures (Figure 32). Preliminary analysis shows impurities on the surface of the sample. These impurities have high contrast and make the vortices and pinning sites hard to detect. More work must be performed to get better samples for measurement.

V.5 Simulating the vortex lattice

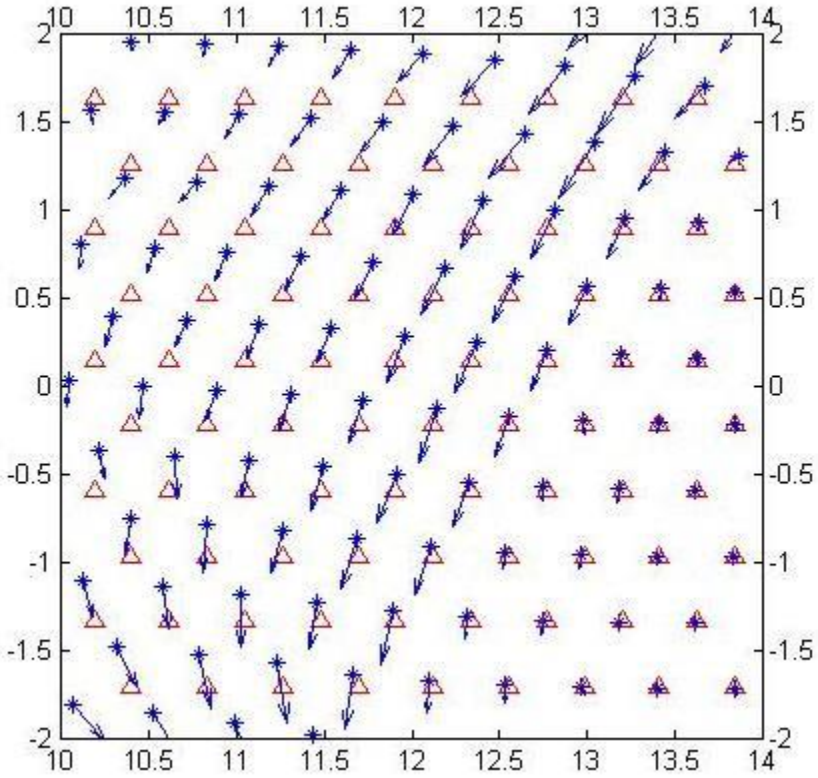

Figure 33. Example of simulation result for the Corbino geometry. The red triangles are the positions of the pinning sites, the blue stars are the positions of the vortices, and the arrows are the velocity vectors for those vortices. There is a dislocation in this vortex lattice causing some vortices to be pinned while others are flowing towards the pinning sites.

Molecular dynamics simulations are a useful tool that allows us to calculate vortex flows with various potential landscapes. Although simulations are not direct evidence of vortex dynamics, they do provide a good tool for predicting vortex behavior and allow us to confirm models based on experimental results.

Molecular dynamics simulations take into account the forces on an object and integrate the motion forward in time based on those forces. This allows us to determine the positions and trajectories of the vortices, and how they interact with periodic potentials such as pinning sites (Figure 33). To perform these simulations there must be a general understanding of the different interactions in the system. In the case of superconducting vortices, the total force on each vortex is the sum of several interactions:

- The force from the vortex – vortex interaction. This is equal to a Bessel function [66] but can be approximated as the Yukawa potential to reduce computation time. This force is summed up over all the vortices around the affected vortex.
- The force from the boundary of the system preventing vortices from leaving. At the boundary a vortex sees a Bean-Livingston barrier repelling it away from the edge [88]. Alternatively a solid boundary can be created using an array of static vortices. For infinite systems, instead of a force, periodic boundary conditions are implemented to prevent the escape of flux from the system.

- A driving force to simulate a current density in the sample. For a linear system the force is equal and uniform in a single direction. For the Corbino geometry (See Chapter IV) it is a tangential force with magnitude 1/R, where R is the distance to the center. This force diverges at the center of the geometry. To remove the singularity (and take into account the finite size of the current injection area) a constant magnitude is used up to some radius (5 μm for a 20 μm total radius). This constant magnitude of force corresponds to a constant magnitude current density, which is equivalent to a linearly increasing current when current density is integrated over a radially symmetric ring.
- The drag force. A moving vortex causes dissipation and loses energy. This loss of energy can be expressed as a drag term where the force is proportional but opposite to the velocity of the vortex, $\overrightarrow{F_d} = -b\,\vec{v}$. When the vortex first accelerates the driving force is dominant. However, after a short period the object reaches terminal velocity where the force term from the velocity is equal to the other force terms causing the acceleration to be zero.
- Pinning interaction. This was expressed either as a Gaussian shaped potential at the center of the pinning site, or as an additional drag term. The addition of drag is justified because of the corrugation of

the Nb around the pinning sites which could force the field lines of the vortex to bend.

If each vortex-vortex interaction is calculated the speed of the algorithm is proportional to the number of vortices squared, $O(N^2)$. In order to increase the speed of the algorithm and change it from an $O(N^2)$ operation, we limit the vortex–vortex interactions and the pinning interactions in length. The simulation area is divided into several small bins and vortices are allowed to interact only with objects in the same or adjacent bins. The bins contents are updated every few steps. This increases the speed of the algorithm and makes it O(N Log(N)).

The algorithm used to perform the calculations is called the Verlet integrator [95]. The algorithm uses the following formula to calculate the positions of each step:

$$\boldsymbol{x_{n+1} = (2 - f)x_n - (1 - f)x_{n-1} + a_n \Delta t^2} \quad \text{(V.1)}$$

Where x_n is the position of a vortex at time step n, f is the fraction of velocity removed due to drag ($f = b\Delta t$, where b is the drag coefficient defined above), a_n is the total acceleration calculated by summing the forces on the vortex (the mass is taken as one), and Δt is the time step. This algorithm also allows us to calculate the velocity of the vortices,

$$v_n = \frac{x_n - x_{n-1}}{\Delta t} \quad \text{(V.2)}$$

which is proportional to the voltage created in the system.

To initialize the system the vortex positions were randomly chosen and the system was allowed to relax without the driving force or pinning interactions. The drag force removes the excess energy from the vortices over time, equivalent to a reduction in temperature. Eventually the lattice settles into either an ordered lattice or a glass with quenched disorder, depending on the strength of the drag term and the vortex-vortex interaction. Once that occurs, the driving force, and later the pinning interactions are enabled.

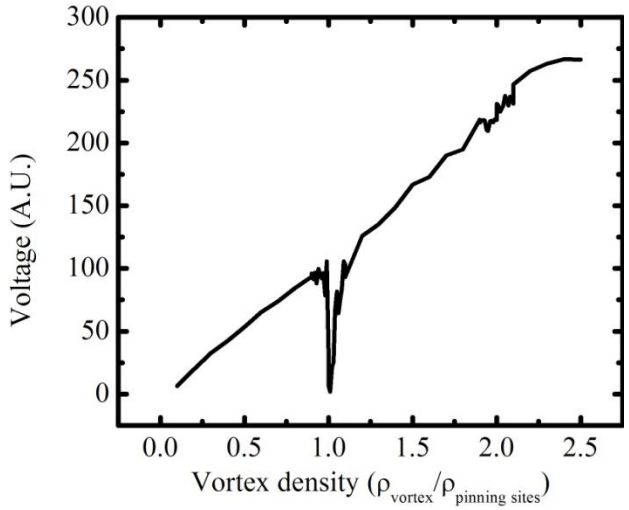

Figure 34. Simulation results giving the voltage as a function of vortex density in the Corbino geometry. The voltage is the sum of the speeds of the vortices. The vortex density is normalized to the density of the pinning sites.

One of the main conclusions from these simulations is that in order to see matching minima in the magneto-resistance simulations, both a drag interaction and an attractive force towards the center of the pinning site were required (Figure 34). Purely an attractive force did not affect the average speed of the vortices, and having purely a drag term did not cause the experimentally observed pinning. Both were

needed in order to attract the vortices to the pinning sites and then remove enough energy from the system to be visible in the voltage curve.

The main goal of these simulations was to simulate the behavior of the vortices in the various potential landscapes described in this dissertation. The behavior and trends of the magneto-resistance curves could not be recreated using the forces described in this chapter. This is probably due to an incomplete description of the forces involved in the superconducting vortex system.

V.6 Acknowledgments

Chapter V contains work performed with several collaborators. I would like to thank Carlos Monton, Ilya Valmianski, and Juan Pererio for the fabrication of the porous alumina. I would like to thank Amos Sharoni for useful conversations and advice in regards to section 'V.1 Pinning boundary effects'. I would also like to thank Stefan Guenon for the conformal mapping experiments. I would like to thank Santiago Carreira, Claudio Chiliotte, and Victoria Bekeris for measurements in regard to section 'V.2 Magnetic susceptibility measurements'. I would like to thank Qiang Wang and Mike Fitzimmonds for measurements in regards to section 'V.3 Neutron scattering'. I would like to thank Sergio Montoya, Matthias Gottwald, and Eric Fullerton for measurements in regard to section 'V.4 Magnetic force microscopy of the vortex lattice'. Finally, I would like to thank Cynthia and Charles Reichhardt for useful conversations and advice in regards to section 'V.5 Simulating the vortex lattice'. Y. J. Rosen performed the fabrication and measurements in V.1. Y. J. Rosen

assisted in the fabrication of the samples, and is providing the theoretical background for section V.2, V.3, and V.4. Y. J. Rosen performed the simulations in V.5.

CHAPTER VI

SUMMARY

Superconducting vortices are a macroscopic quantum mechanical system with length scales that can be reached using nanolithography techniques. The vortex potential energy landscape can be manipulated using artificial pinning sites and various current distributions. These tools allow the study of collective vortex motion, and offer a wide range of applications. This dissertation studies commensurability effects with disordered lattices, rectification and switching devices, and several ongoing studies using a variety of measurement techniques.

When the vortex-vortex interaction is strong compared to other forces, the vortices arrange themselves into a triangular lattice (section I.2.2 Superconducting vortices). However, in the presence of disordered pinning sites, the vortex lattice contains dislocations and defects. In Chapter II, artificial pinning sites configured using the two-dimensional parking algorithm allowed control over the amount of order in the pinning lattice. The most ordered realization of the algorithm showed matching effects, meaning the vortices could collectively interact with the pinning sites. As the order in the pinning lattice was reduced, the collective vortex interaction with that lattice was lessened. However, magneto-resistance minima were seen even when the pinning site order was very short. The optimal pinning condition, which is normally set only by the pinning site density, did not occur at the matching field.

Instead, it was reached at lower magnetic fields. The short range of order suppressed the ability of the vortex lattice to interact with the pinning lattice at higher densities. It is interesting to note that there were small interactions at higher magnetic fields. These could be due to ordered structures repeating in the pinning lattice.

The matching minima could also be moved to higher fields by randomly removing pinning sites from an ordered lattice. By diluting the pinning lattice, the density was reduced while still maintaining the same lattice parameter. In this experiment, the optimal pinning condition occurred when the vortices had a higher density than the pinning lattice. This means the vortex lattice had an order imposed upon it that would not be there without the pinning sites. However, it is believed that there is a limit to this imposed order, which relates to the percolation threshold when diluting the pinning arrays.

There are several devices proposed that use superconducting vortices. In Chapter III the ratchet effect is explored. When vortices interact with asymmetric pinning sites they show a preferred direction of motion. The preferred direction is due to the geometry of the individual pinning sites and to their lattice configuration. Depending on the density of the vortex lattice, the preferred direction can be reversed and an opposite ratchet effect can be achieved. In a triangular lattice of triangular pinning sites, this reversal implies that there are dynamically generated interstitial vortices trapped outside the pinning sites. The geometry of the pinning sites funnels them in a zigzag motion, which gives a preferred direction and causes a

rectification of their motion. At high current amplitudes, the vortices can re-enter the pinning sites and so the shape of those pinning sites dominates the rectification effects.

The vortex lattice flow can be manipulated by altering the current distribution in addition to the pinning lattice. In the Corbino geometry, discussed in Chapter IV, current enters at the center of a disc and travels radially outwards. In this configuration, the vortices feel a force perpendicular to the current, which causes them to rotate in a circle. Depending on the temperature, either the vortices can rotate in individual rings, or they can rotate elastically as a rigid lattice. When we place pinning sites in this system, vortices on the outer edge experience higher drag than the central vortices due to their higher speeds. When the vortex lattice is at the maximum drag condition (the matching field), it shears. This causes a sharp increase in speed, which translates into a step in the resistance. The dynamics can be reversed by reducing the field again and having the inner vortices lock to the outer vortices. In this way, two different regimes of vortex flow can be measured by changing the field very slightly over the transition. This has possible applications towards a switching device with discretized resistances.

Chapter V describes various ongoing experiments performed on vortex lattices. When the density of the pinning site lattice was varied, commensurability effects occurred even in the presence of other length scales. The vortex lattice only interacted with lattice parameters similar to itself. Neutron scattering experiments

may allow the determination of order in the vortex lattice, and shed light on interactions with the pinning sites. Microwave measurements are used to probe the pinning strength, and determine the repulsion of the vortices from superconducting dots. Magnetic force microscopy can be used to directly visualize the positions of the static vortices and see how they interact with individual pinning sites. Finally, simulations can reproduce matching minima, but the Hamiltonian is likely missing interaction terms crucial to the recovery of vortex dynamics.

In this dissertation several important questions have been studied regarding disorder and the vortex lattice, the origin of the ratchet effect, and the shearing conditions of the vortex lattice. The results could potentially be used for superconducting diodes or switches, reducing noise in superconducting systems, and understanding analogous periodic systems. The rich and novel physics that can be explored using superconducting vortices is virtually unlimited and offers numerous potential applications.

BIBLIOGRAPHY

[1] M. Tinkham, *Introduction to Superconductivity* (McGraw-Hill, New York, NY, 1996).

[2] R. P. Huebener, *Magnetic Flux Structures in Superconductors* (Springer, New York, NY, 1979).

[3] Y. Makhlin, G. Schön, and A. Shnirman, Reviews of Modern Physics **73**, 357 (2001).

[4] A. Catana, J. P. Locquet, S. M. Paik, and I. K. Schuller, Physical Review B **46**, 15477 (1992).

[5] C. F. Driscoll, D. Z. Jin, D. A. Schecter, and D. H. E. Dubin, Physica C: Superconductivity **369**, 21 (2002).

[6] R. D. Astumian, Science **276**, 917 (1997).

[7] M. Lange, M. J. Van Bael, Y. Bruynseraede, and V. V. Moshchalkov, Physical Review Letters **90**, 197006 (2003).

[8] J. E. Villegas, C.-P. Li, and I. K. Schuller, Physical Review Letters **99**, 227001 (2007).

[9] J. E. Villegas, S. Savel'ev, F. Nori, E. M. Gonzalez, J. V Anguita, R. García, and J. L. Vicent, Science **302**, 1188 (2003).

[10] A. Gilabert, I. K. Schuller, V. V. Moshchalkov, and Y. Bruynseraede, Applied Physics Letters **64**, 2885 (1994).

[11] P. W. Anderson and N. Itoh, Nature **256**, 25 (1975).

[12] L. Civale, A. D. Marwick, T. K. Worthington, M. Kirk, J. Thompson, L. Krusin-Elbaum, Y. Sun, J. Clem, and F. Holtzberg, Physical Review Letters **67**, 648 (1991).

[13] E. H. Brandt, Reports on Progress in Physics **58**, 1465 (1995).

[14] P. Selders and R. Wördenweber, Applied Physics Letters **76**, 3277 (2000).

[15] B. R. Weinberger, L. Lynds, and J. R. Hull, Superconductor Science and Technology **3**, 381 (1990).

[16] O. M. Corbino, Il Nuovo Cimento **1**, 397 (1911).

[17] P. G. De Gennes, *Superconductivity of Metals and Alloys* (W. A. Benjamin, Inc., New York, NY, 1966).

[18] A. Hoffmann, P. Prieto, and I. K. Schuller, Physical Review B **61**, 6958 (2000).

[19] T. Matsushita, *Flux Pinning in Superconductors* (Springer Berlin Heidelberg, Berlin, Heidelberg, 2007).

[20] D. S. Fisher, M. P. A. Fisher, and D. A. Huse, Physical Review B **43**, 130 (1991).

[21] H. F. Hess, R. B. Robinson, R. C. Dynes, J. M. Valles Jr., and J. V. Waszczak, Physical Review Letters **62**, 214 (1989).

[22] C. Reichhardt, C. J. Olson, and F. Nori, Physical Review B **57**, 7937 (1998).

[23] Y. Jaccard, J. I. Martin, M.-C. Cyrille, M. Velez, J. L. Vicent, and I. K. Schuller, Physical Review B **58**, 8232 (1998).

[24] J. I. Martin, M. Velez, J. Nogues, and I. K. Schuller, Physical Review Letters **79**, 1929 (1997).

[25] J. I. Martín, M. Vélez, A. Hoffmann, I. K. Schuller, and J. L. Vicent, Physical Review B **62**, 9110 (2000).

[26] J. E. Villegas, E. M. González, M. I. Montero, I. K. Schuller, and J. L. Vicent, Journal of Physics and Chemistry of Solids **67**, 482 (2006).

[27] D. J. Morgan and J. B. Ketterson, Physical Review Letters **80**, 3614 (1998).

[28] T. C. Wu, J. C. Wang, L. Horng, J. C. Wu, and T. J. Yang, Journal of Applied Physics **97**, 10B102 (2005).

[29] M. Kemmler, C. Gürlich, A. Sterck, H. Pöhler, M. Neuhaus, M. Siegel, R. Kleiner, and D. Koelle, Physical Review Letters **97**, 147003 (2006).

[30] R. B. G. Kramer, A. V. Silhanek, J. Van de Vondel, B. Raes, and V. V. Moshchalkov, Physical Review Letters **103**, 067007 (2009).

[31] J. E. Villegas, M. I. Montero, C.-P. Li, and I. K. Schuller, Physical Review Letters **97**, 027002 (2006).

[32] A. Hoffmann, P. Prieto, V. Metlushko, and I. K. Schuller, Journal of Superconductivity and Novel Magnetism **25**, 2187 (2012).

[33] A. Hoffmann, L. Fumagalli, N. Jahedi, J. C. Sautner, J. E. Pearson, G. Mihajlović, and V. Metlushko, Physical Review B **77**, 060506 (2008).

[34] C.-P. Li, I. V. Roshchin, X. Batlle, M. Viret, F. Ott, and I. K. Schuller, Journal of Applied Physics **100**, 074318 (2006).

[35] J. P. O'Sullivan and G. C. Wood, Proceedings of the Royal Society A: Mathematical, Physical and Engineering Sciences **317**, 511 (1970).

[36] H. Masuda and M. Satoh, Japanese Journal of Applied Physics **35**, L126 (1996).

[37] S. Chapman and T. G. Cowling, *The Mathematical Theory of Non-uniform Gases: An Account of the Kinetic Theory of Viscosity, Thermal Conduction and Diffusion in Gases* (Cambridge University Press, New York, NY, 1970), p. 423.

[38] A. Daire, W. Goeke, and M. A. Tupta, *White Paper: New Instruments Can Lock Out Lock-ins* (Keithley Instruments, Inc., Cleveland, OH, 2005).

[39] P. A. Lee and T. V. Ramakrishnan, Reviews of Modern Physics **57**, 287 (1985).

[40] T. Saerbeck, F. Klose, D. Lott, G. J. Mankey, Z. Lu, P. R. LeClair, W. Schmidt, A. P. J. Stampfl, S. Danilkin, M. Yethiraj, and A. Schreyer, Physical Review B **82**, 134409 (2010).

[41] K. Binder and A. P. Young, Reviews of Modern Physics **58**, 801 (1986).

[42] O. Daldini, P. Martinoli, J. L. Olsen, and G. Berner, Physical Review Letters **32**, 218 (1974).

[43] A. P. Li, F. Muller, A. Birner, K. Nielsch, and U. Gosele, Journal of Applied Physics **84**, 6023 (1998).

[44] S. X. Dou, S. Soltanian, J. Horvat, X. L. Wang, S. H. Zhou, M. Ionescu, H. K. Liu, P. Munroe, and M. Tomsic, Applied Physics Letters **81**, 3419 (2002).

[45] D. M. Silevitch, D. H. Reich, C. L. Chien, S. B. Field, and H. Shtrikman, Journal of Applied Physics **89**, 7478 (2001).

[46] C. Reichhardt, J. Groth, C. J. Olson, S. B. Field, and F. Nori, Physical Review B **54**, 16108 (1996).

[47] X. Hallet, M. Mátéfi-Tempfli, S. Michotte, L. Piraux, J. Vanacken, V. V Moshchalkov, and S. Mátéfi-Tempfli, Small **5**, 2413 (2009).

[48] J. Eisenmenger, M. Oettinger, C. Pfahler, A. Plettl, P. Walther, and P. Ziemann, Physical Review B **75**, 144514 (2007).

[49] M. Trezza, S. L. Prischepa, C. Cirillo, R. Fittipaldi, M. Sarno, D. Sannino, P. Ciambelli, M. B. S. Hesselberth, S. K. Lazarouk, a. V. Dolbik, V. E. Borisenko, and C. Attanasio, Journal of Applied Physics **104**, 083917 (2008).

[50] W. Vinckx, J. Vanacken, V. V. Moshchalkov, S. Mátéfi-Tempfli, M. Mátéfi-Tempfli, S. Michotte, L. Piraux, and X. Ye, Physica C **459**, 5 (2007).

[51] C. Chiliotte, G. Pasquini, V. Bekeris, J. E. Villegas, C.-P. Li, and I. K. Schuller, Superconductor Science and Technology **24**, 065008 (2011).

[52] H. Solomon, in *Proceedings of the Fifth Berkeley Symposium on Mathematical Statistics and Probability, Vol. III: Physical Sciences* (University of California Press, Berkeley, California, 1967).

[53] J. Feder, Journal of Theoretical Biology **87**, 237 (1980).

[54] E. R. Weeks, *What is the pair correlation function g(r)?*, 2006. [Online]. Available: http://www.physics.emory.edu/~weeks/idl/gofr.html. [Accessed: 26-Jun-2012].

[55] J. M. Ziman, *Models of Disorder: The Theoretical Physics of Homogeneously Disordered Systems* (Cambridge University Press, Cambridge, New York, 1979).

[56] A. T. Fiory, A. F. Hebard, and S. Somekh, Applied Physics Letters **32**, 73 (1978).

[57] E. Brandt, Physical Review B **34**, 6514 (1986).

[58] M. Kemmler, D. Bothner, K. Ilin, M. Siegel, R. Kleiner, and D. Koelle, Physical Review B **79**, 184509 (2009).

[59] C. Reichhardt and C. J. O. Reichhardt, Physical Review B **76**, 094512 (2007).

[60] S. R. Finch, *Mathematical Constants*, illustrate (Cambridge University Press, Camridge, United Kingdom, 2003).

[61] A. L. Wells, A. W. Lin, L. Q. Chen, D. Safer, S. M. Cain, T. Hasson, B. O. Carragher, R. A. Milligan, and H. L. Sweeney, Nature **401**, 505 (1999).

[62] A. S. Sedra and K. C. Smith, *Microelectronic Circuits*, Fifth (Oxford University Press, Oxford, New York, 2004).

[63] W. Gillijns, A. V. Silhanek, V. V. Moshchalkov, C. J. O. Reichhardt, and C. Reichhardt, Physical Review Letters **99**, 247002 (2007).

[64] M. Vélez, J. I. Martín, J. E. Villegas, A. Hoffmann, E. M. González, J. L. Vicent, and I. K. Schuller, Journal of Magnetism and Magnetic Materials **320**, 2547 (2008).

[65] L. Dinis, E. M. González, J. V Anguita, J. M. R. Parrondo, and J. L. Vicent, New Journal of Physics **9**, 366 (2007).

[66] Q. Lu, C. J. O. Reichhardt, and C. Reichhardt, Physical Review B **75**, 054502 (2007).

[67] D. Perez de Lara, M. Erekhinsky, E. M. Gonzalez, Y. J. Rosen, I. K. Schuller, and J. L. Vicent, Physical Review B **83**, 17 (2011).

[68] C. Caroli and K. Maki, Physical Review **164**, 591 (1967).

[69] C. Reichhardt and C. J. O. Reichhardt, Physical Review B **81**, 024510 (2010).

[70] J. E. Villegas, E. M. Gonzalez, M. I. Montero, I. K. Schuller, and J. L. Vicent, Physical Review B **72**, 064507 (2005).

[71] K. Kadowaki, Science and Technology of Advanced Materials **6**, 589 (2005).

[72] E. Altshuler, T. H. Johansen, Y. Paltiel, P. Jin, K. E. Bassler, O. Ramos, Q. Y. Chen, G. F. Reiter, E. Zeldov, and C. W. Chu, Physical Review B **70**, 140505 (2004).

[73] I. Giaever, Physical Review Letters **15**, 825 (1965).

[74] C. J. O. Reichhardt and C. Reichhardt, Physical Review B **81**, 224516 (2010).

[75] M. Shaw and P. Solomon, Physical Review **164**, 535 (1967).

[76] D. López, W. Kwok, H. Safar, R. Olsson, A. Petrean, L. Paulius, and G. Crabtree, Physical Review Letters **82**, 1277 (1999).

[77] P. Benetatos and M. C. Marchetti, Physical Review B **65**, 134517 (2002).

[78] N. S. Lin, T. W. Heitmann, K. Yu, B. L. T. Plourde, and V. R. Misko, Physical Review B **84**, 144511 (2011).

[79] N. S. Lin, V. R. Misko, and F. M. Peeters, Physical Review B **81**, 134504 (2010).

[80] S. Okuma, Y. Tsugawa, and A. Motohashi, Physical Review B **83**, 012503 (2011).

[81] T. W. Heitmann, K. Yu, C. Song, M. P. DeFeo, B. L. T. Plourde, M. B. S. Hesselberth, and P. H. Kes, The Review of Scientific Instruments **79**, 103906 (2008).

[82] N. S. Lin, V. R. Misko, and F. M. Peeters, Physical Review Letters **102**, 197003 (2009).

[83] C. Reichhardt and N. Grønbech-Jensen, Physical Review B **63**, 054510 (2001).

[84] C. J. Olson, C. Reichhardt, J. Groth, S. B. Field, and F. Nori, Physica C: Superconductivity **290**, 89 (1997).

[85] D. Ray, C. J. O. Reichhardt, B. Janko, and C. Reichhardt, arXiv: 1210.1229 (2012).

[86] W. A. Little and R. D. Parks, Physical Review Letters **9**, 9 (1962).

[87] B. D. Josephson, Physics Letters **1**, 251 (1962).

[88] C. Bean and J. Livingston, Physical Review Letters **12**, 14 (1964).

[89] S. Field, J. Witt, F. Nori, and X. Ling, Physical Review Letters **74**, 1206 (1995).

[90] C. Chiliotte, D. Pérez Daroca, G. Pasquini, V. Bekeris, C.-P. Li, F. Casanova, J. E. Villegas, and I. K. Schuller, Physica B: Condensed Matter **404**, 2809 (2009).

[91] A. M. Campbell and J. E. Evetts, Advances in Physics **50**, 1249 (2001).

[92] J. R. Hull and M. Murakami, Proceedings of the IEEE **92**, 1705 (2004).

[93] X. Wang, H. A. Hanson, X. S. Ling, C. F. Majkrzak, and B. B. Maranville, Journal of Applied Crystallography **44**, 414 (2011).

[94] J. R. Kirtley, Reports on Progress in Physics **73**, 126501 (2010).

[95] M. P. Allen and D. J. Tildesley, *Computer Simulation of Liquids* (Oxford University Press, New York, 1987).